The dopants and doping level dependence of the structure and magnetic properties of the Eu $(Ba_{1-x}LR_x)_2Cu_3O_{7+\delta}$ system

by

Yu Lin

A thesis submitted to the graduate faculty

in partial fulfillment of the requirements for the degree of

MASTER OF SCIENCE

Major: Materials Science and Engineering

Program of Study Committee
R. W. McCallum (Co-major professor)
M. J. Kramer (Co-major professor)
D. K. Finnemore

Iowa State University

Ames, Iowa

2001

Graduate College
Iowa State University

This is to certify that the Master's thesis of

Yu Lin

has met the thesis requirements of Iowa State University

_____
Co-major Professor

_____
Co-major Professor

_____
For the Major Program

TABLE OF CONTENTS

ABSTRACT v

CHAPTER 1. INTRODUCTION 1

1.1 Conventional Superconductors 3

1.2 High T_c Superconductors 11

CHAPTER 2. LITERATURE REVIEW 14

2.1 Conduction Mechanism of High T_c Superconductors 14

2.2 Crystal Structures 15

2.3 Important Characteristics 16

2.3.1 Critical transition temperature (T_c) 16

2.3.2 Critical current density (J_c) 19

2.3.3 Upper critical field (H_{c2}) 24

2.4 Vortex Flux Pinning 25

2.4.1 Vortex state 25

2.4.2 Flux pinning 27

2.5 Summary 28

CHAPTER 3. METHODS 31

3.1 Materials Preparation 31

3.2 Characterization 38

3.2.1 Differential thermal analysis (DTA) 38

3.2.2 X-ray diffraction (XRD) 38

3.2.3 Magnetic properties 39

3.2.3.1 DC SQUID (Superconducting QUantum Interference Device) 39

3.2.3.2 Characterization of critical transition temperature 40

3.2.3.3 Characterization of critical current density 42

3.2.3.4 Characterization of upper critical field 42

CHAPTER 4. RESULTS AND DISCUSSIONS 45

4.1 Crystal Structures of $Eu(Ba_{1-x}Nd_x)_2Cu_3O_{7+\delta}$ 45

4.2 Critical Transition Temperature of $Eu(Ba_{1-x}Nd_x)_2Cu_3O_{7+\delta}$ 50

4.3 Critical Current Density of $Eu(Ba_{1-x}LR_x)_2Cu_3O_{7+\delta}$ 50

4.4 Irreversibility Line of $Eu(Ba_{1-x}LRx)_2Cu_3O_{7+\delta}$ 53

CHAPTER 5. CONCLUSIONS 66

REFERENCES 71

ACKNOWLEDGEMENTS 74

IS-T 2102

ABSTRACT

$Eu(Ba_{1-x}Nd_x)_2Cu_3O_{7+\delta}$ were systematically studied in order to understand how the valence of the rear earth elements, ionic sizes and magnetic moment affect the crystal structure and magnetic and electrical properties. Differential thermal analyses were carried out to check the phase purity, X-ray data were least-squares fitted to determine the lattice parameters, and DC - SQUID magnetometry was used to characterize the superconducting properties. These results showed that the crystallography is consistent with other EuLR123ss series, LR = La, Pr, Eu. The lattice parameters vary with the ionic radii of the rare earth ions.

Unlike the uniform change in lattice parameter, the superconducting transition did not vary systematically with the ionic size of the dopants. Although the general trend was for T_c to decrease with decreasing ionic size of the dopant, for the same doping level, Pr was anomalous, depressing T_c faster. Although the exact mechanism is not clear, this result is consistent with the depression of T_c for Pr substitution for the rare earth in R123.

The critical current J_c was determined using the Bean model from magnetization versus field measurements as a function of temperature and field. The effect of the dopants on J_c with the increasing of temperature or applied field was determined. For $T < 77$ K and small values of x, the value of J_c was increased over that of the $x = 0$ sample. In addition, the smaller the substituting atom, the higher the J_c becomes. For instance, at $x = 0.025$, Eu123 < EuLa.025 < EuPr.025 < EuNd.025 < EuEu.025. The enhancement of J_c disappears for $x > 0.05$ and $T > 0.5T_c$.

In order to further understand of the effect of dopants on flux pinning, the value of the upper critical field, H_{c2}, must be accurately known for each sample. However, this proved to be very difficult due to the Eu moment and the polycrystalline nature of these samples. Even though highly aligned samples were obtained, the alignment process introduced added contributions to the magnetization due to the epoxy and Cu cube which were used. These contributions introduce an uncertainty in the background correction on the order of 0.1% of the change in magnetization associated with the superconducting transition. Unfortunately near T_c this uncertainty is too large for the successful application of the Hao-Clem model used to determine H_{c2}. The aligned samples did allow for the determination of the anisotropy in T_c and the temperature dependence of the irreversibility line near T_c. Stoichiometric 123 has the smallest T_c depression as a function of applied field with the field dependency increasing with increasing dopant levels. These results indicate that the point–like-defects caused by rare earth ions on the Ba site are not effective at pinning the flux lattice near the irreversibility line. Although the critical current is enhanced far away from this region of flux melting, the thermal motion of the flux lattice near T_c is too large to be pinned by these types of defects.

CHAPTER 1. INTRODUCTION

In 1908, H. K. Onnes first liquefied helium. Because of this refrigeration technique, he could get temperature as low as few Kelvin (K). In 1919, H. K. Onnes observed that when cooled, the electrical resistance of mercury dropped sharply to zero at 4.15 K over a temperature interval of 0.01K [1, 2], (Figure 1.1a). Before this, all conductors were believed to have finite resistance. Materials with zero electrical resistance are called superconductors. In the subsequent decades, numerous materials were shown to superconduct at very low temperatures. In fact, later, after detailed measurements, people found that superconductors have very small resistance, which is less than $10^{-21}\Omega$ cm. This "perfect" conductivity without resistance is the first characteristic of superconductivity. Another characteristic is total diamagnetism found by Meissner and Ochesenfeld in 1933 [3]. When a magnetic field is applied, the superconductor at temperature below a critical temperature, T_c, will expel the magnetic flux completely as if the magnetic induction inside the specimen $B = 0$. Even if the sample is cooled down through T_c, the flux originally presented will be also rejected from the sample.

The establishment of the energy gap theory by Daunt and Mendelssohn [4] enabled a better understanding of superconductors. It states that there exits an energy difference between the ground state and excitation state of system. Specific heat experiments (Figure 1.1b) and measurements of electromagnetic absorption in the region of $h\nu \sim \kappa T_c$ by Corak et. al. [5] were consistent with this theory.

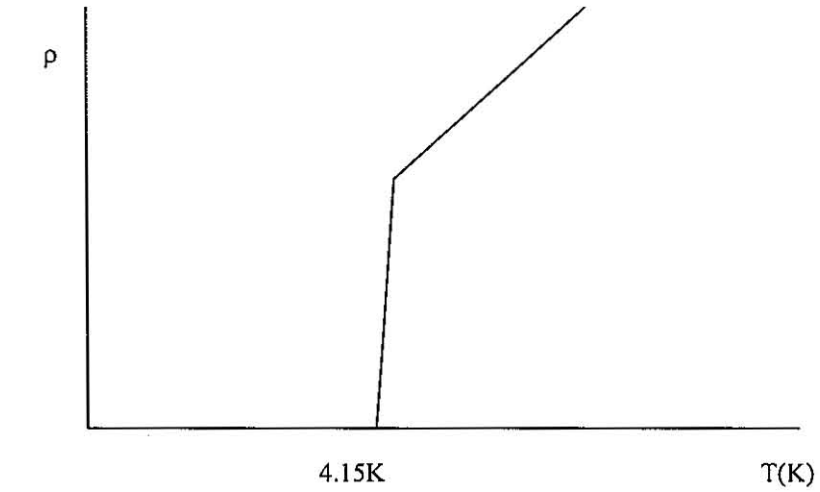

(a)

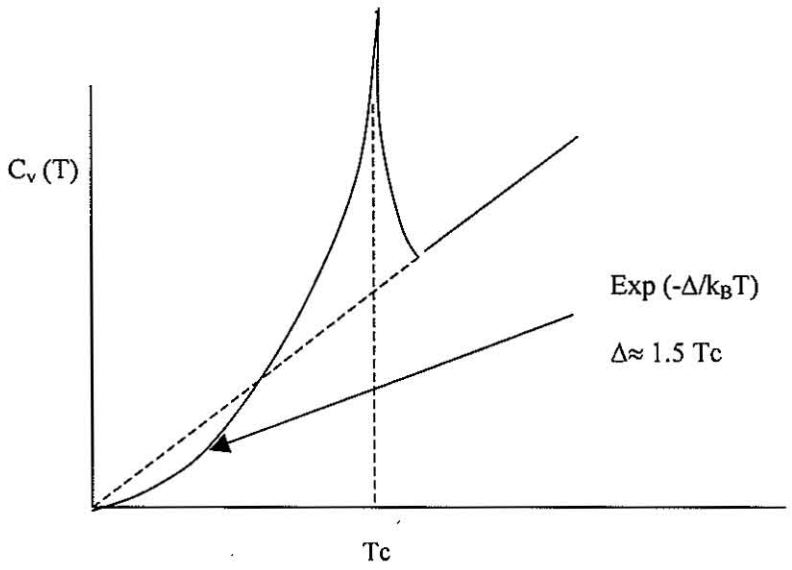

(b)

Figure 1.1 (a) the resistivity-temperature curve of mercury, $\rho\ (T < T_c) < 10^{-17}\rho\ (T_c+\delta)$; (b) the heat capacitance of the mercury

In 1957, Bardeen, Cooper and Schrieffer [6] proposed that the formation of bound pairs of electrons occupying states with equal and opposite momentum and spins explains the decrease in the system energy. Under these conditions, ordinary Fermi ground state of the electron gas would be unstable. The weak attractive interaction is caused in second-order by electron-phonon interaction between the two electrons of a pair.

In 1950, Ginzburg and Laundau [7] introduced a complex pseudowave function Ψ as an order parameter. The Ginzburg-Laundau theory (GL theory) showed that in the intermediate state, superconducting and normal domains could coexist in the presence of a magnetic field above lower critical field (H_{c1}). GL theory is now universally accepted, which embodies the macroscopic quantum-mechanical nature of the superconducting state in a simple way. The two important parameters are the coherence length (ξ) and the penetration depth (λ). ξ is roughly the size of Cooper pair. This sets the minimum distance in which the density of superconductor electrons changes from the value of the bulk superconductor to zero. λ is a measure of the distance away from the normal boundary moving into superconductor, in which the magnetic induction decays exponentially.

1.1 Conventional Superconductors

Superconductors are classified into two types, i.e. type I and type II superconductors. Although there are some exceptions, pure metals tend to be type I superconductors and alloys tend to be type II superconductors [8-12]. The GL parameter $\kappa = \lambda/\xi$ is a good metric to determine the type of superconductor. In 1957, Abrikosov [13] proposed that material with

$\xi < \lambda$ have negative surface energy between the normal and supercondutor states, where the material breaks into superconducting and normal regime which are finely divided as determined by Quantum Mechanics and flux quantization. The size of these regions is limited by ξ. Abrikosov also noted that the breakpoint is $\kappa = \frac{1}{\sqrt{2}}$. In the case of $\kappa < \frac{1}{\sqrt{2}}$, an applied field sufficiently strong to destroy the superconductivity is denoted as H_c, which is temperature-dependent. When magnetic field approaches H_c, the magnetization abruptly drops down to zero, which is a first–order transition. This is a type I superconductor. If $\kappa > \frac{1}{\sqrt{2}}$, there are two critical fields. At the first critical field or lower critical field (H_{c1}), the flux line penetrates the sample. At the second critical field or upper critical field (H_{c2}) [8-12], the superconductivity disappear. This is a type II superconductor. H_{c1} is usually very low, which is less than a few hundred Oe. Only Type II superconductor can be used for applications. A clear picture of the relationship between κ and two types of superconductors is given in Figure 1.2. Figure 1.3 shows the magnetization vs. applied field curve for each type of superconductors. For type I superconductor, there are two states, i.e. Meissner and normal states. Besides these states, type II has one more state: vortex state, which starts from $H = H_{c1}$ and ends at $H = H_{c2}$

Between H_{c1} and H_{c2}, there exists a so-called mixed state, where the penetrating flux lines form a regular array of flux tubes, each of which carry a flux quantum of $\Phi_0 = 2.07E^{-7}$ gauss-cm^2. The phase diagram for different types of superconductors are plotted in Figure 1.4. When the superconductor is in the vortex state, within each grain there are vortices with supercurrent circulating around the flux and squeezing it toward the center.

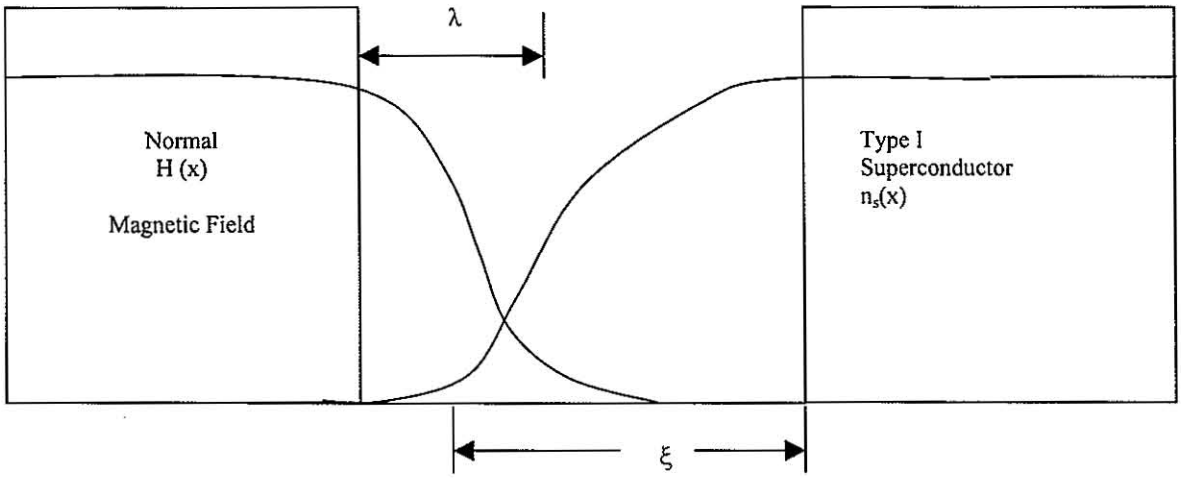

(a)

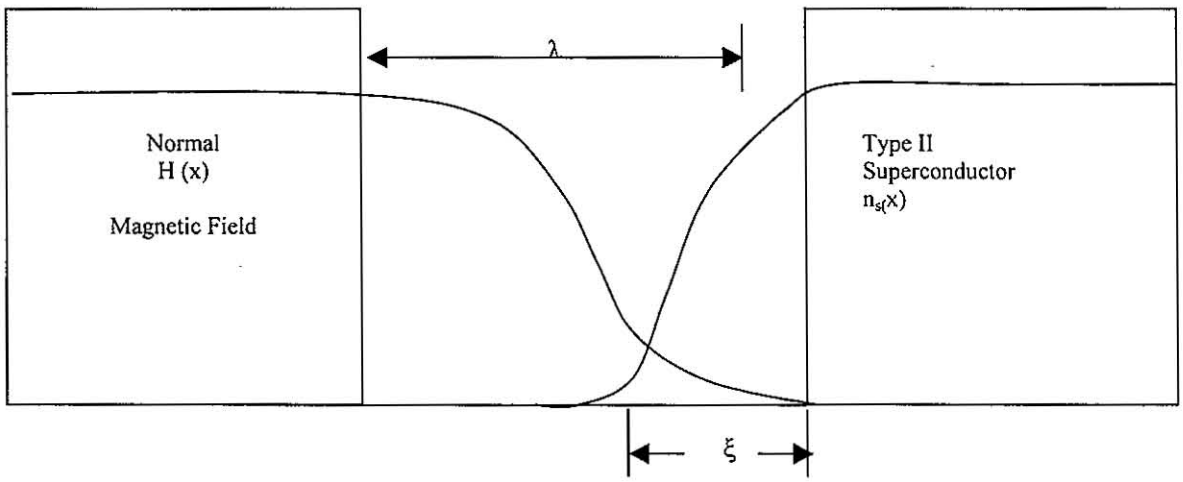

(b)

Figure 1.2 The magnetic field and superconducting electrons density n_s at the boundary between normal region and superconductor region.(a) type I; (b) type II .

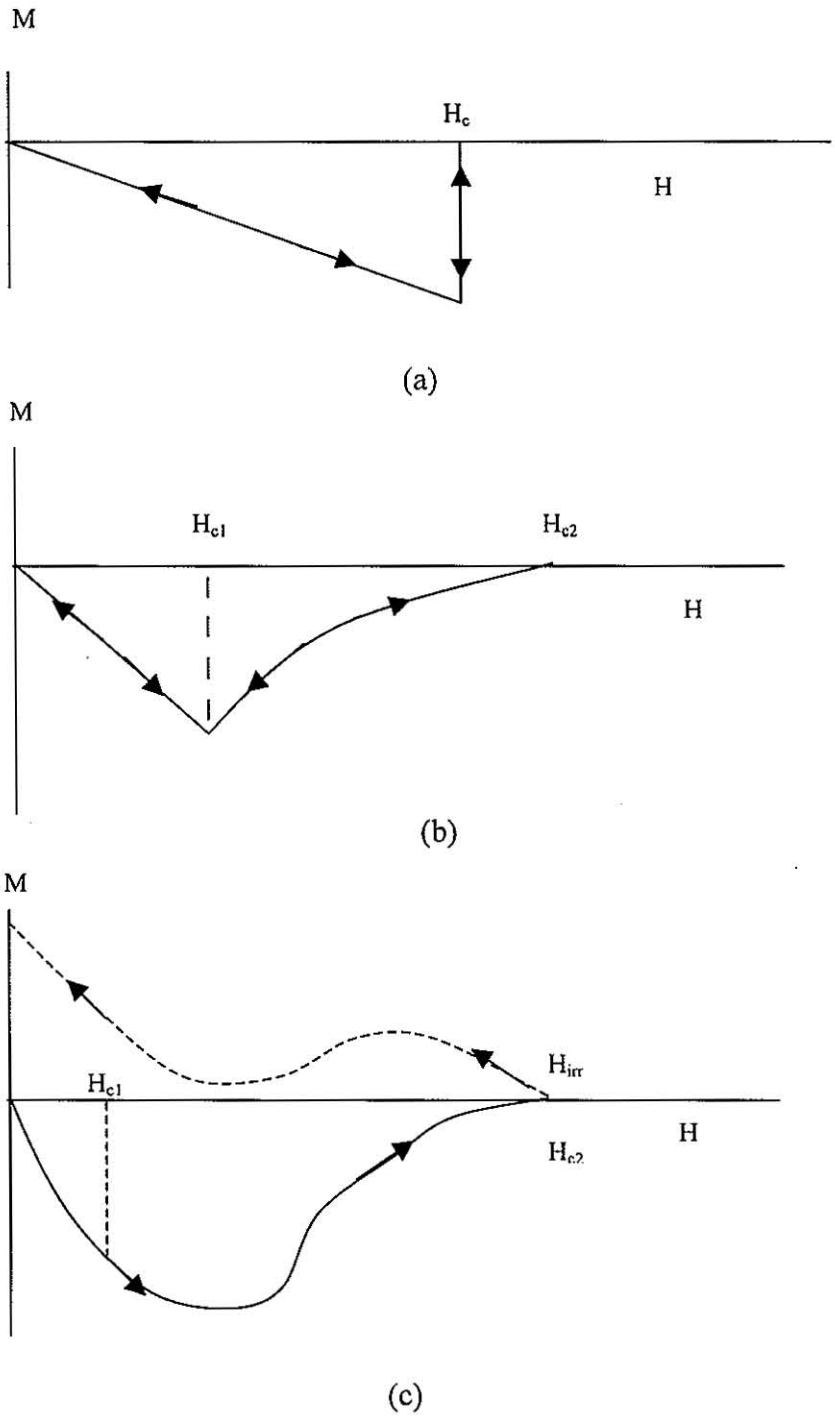

Figure 1.3 Hysteresis of superconductors (a) type I; (b) ideal conventional type II; (c) realistic conventional type II superconductor with irreversible magnetization

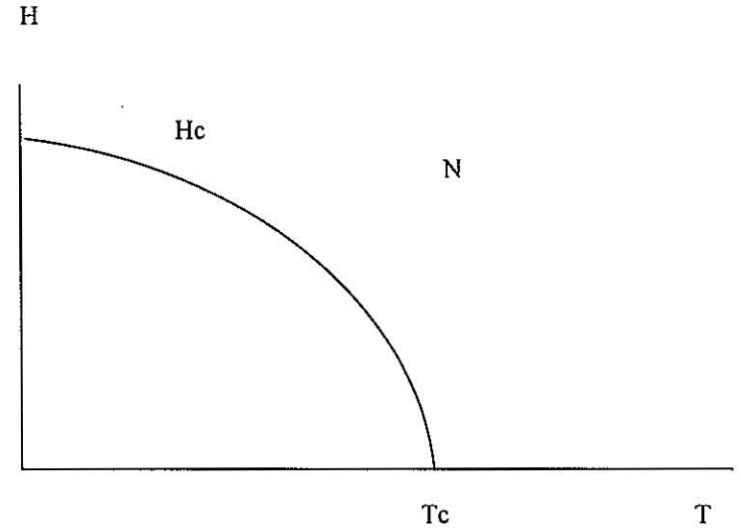

(a)

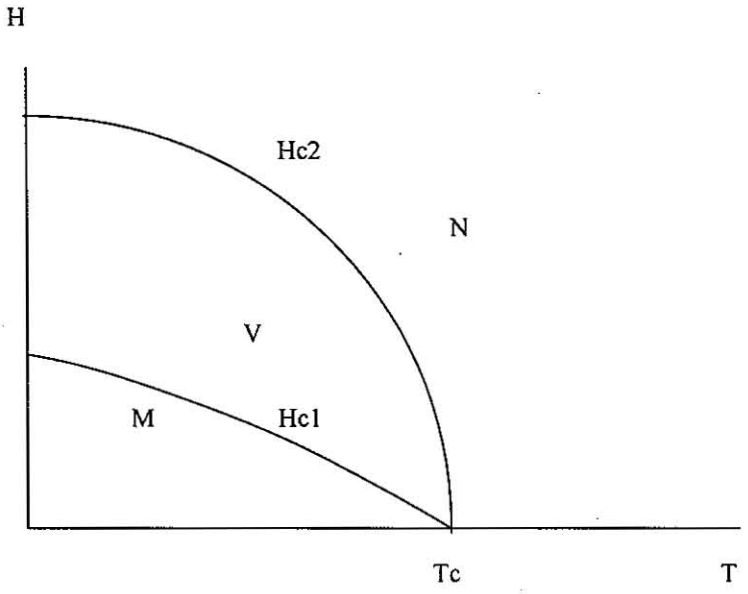

(b)

Figure 1.4 State diagrams for superconductors (a) type I; (b) conventional Type II; M represents Meissner state, V for vortex state, N for normal state.

Figure 1.5a shows a typical Abrikosov vortex structure. Figure 1.5b illustrates the order parameter distribution along the radius of the vortex. Since the superconducting electron density (SED) is the square of the order parameter, this figure also gives an idea of the distribution of the SED. Figure 1.5c shows the supercurrent density around the vortex. A triangular array has the lowest energy [8-12], which was demonstrated experimentally by magnetic decoration technique coupled with electronic microscopy.

In an ideal homogenous material, flux flow is resisted only by a viscous drag. In real material, impurities may pin the flux, so there is no resistance until a finite current is reached. Therefore, introducing defects is one means of enhancing the critical current density.

Typically, type I superconductors occur in material with low T_c. According to equation (1.1), it has large ξ.

$$\xi = \frac{h v_F}{2\pi k_B T_c} \qquad \text{equ. (1.1)}$$

By contrast, type II superconductor has small ξ and large κ. Equation (1.2) and (1.3) provides the relationships between H_{c1} and H_c, H_{c2} and H_c.

$$H_{c1} = \frac{\Phi_0}{4\pi\lambda^2}\ln\kappa = \frac{H_c}{\sqrt{2}}\ln\kappa \qquad \text{equ. (1.2)}$$

$$H_{c2} = \frac{\Phi_0}{2\pi\xi^2} = \sqrt{2}\kappa\ H_c \qquad \text{equ. (1.3)}$$

Actually, because of the demagnetizing effects [14], the flux collapses in a bulk sample within a finite field region instead of at H_c for type I superconductors. The demagnetizing factor is denoted as δ. Flux starts to collapse at $H_a = (1 - \delta) H_c$ and finishes at

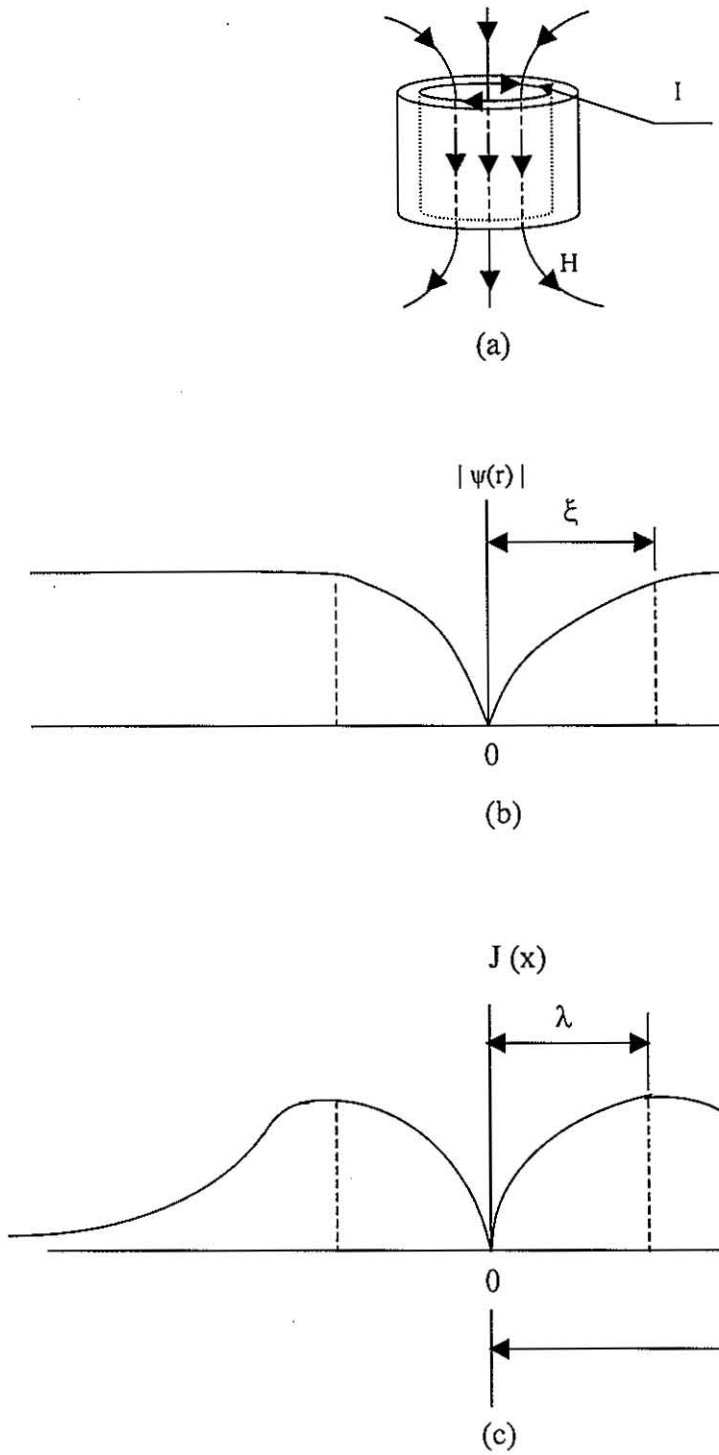

Figure 1.5 Structure of an Abrikosov vortex (a) the vortex; (b) the order parameter; (c) the supercurrent density

H_c. Here, δ is sample shape dependent. For example, a long rod sample with magnetic field parallel to the long axis of the rod has $\delta \approx 0$; a sphere has $\delta = 1/3$; a flat sample slab with magnetic field perpendicular to the slab has $\delta \approx 1$. Figure 1.6 showed how the sample shape influences the M vs. H curve.

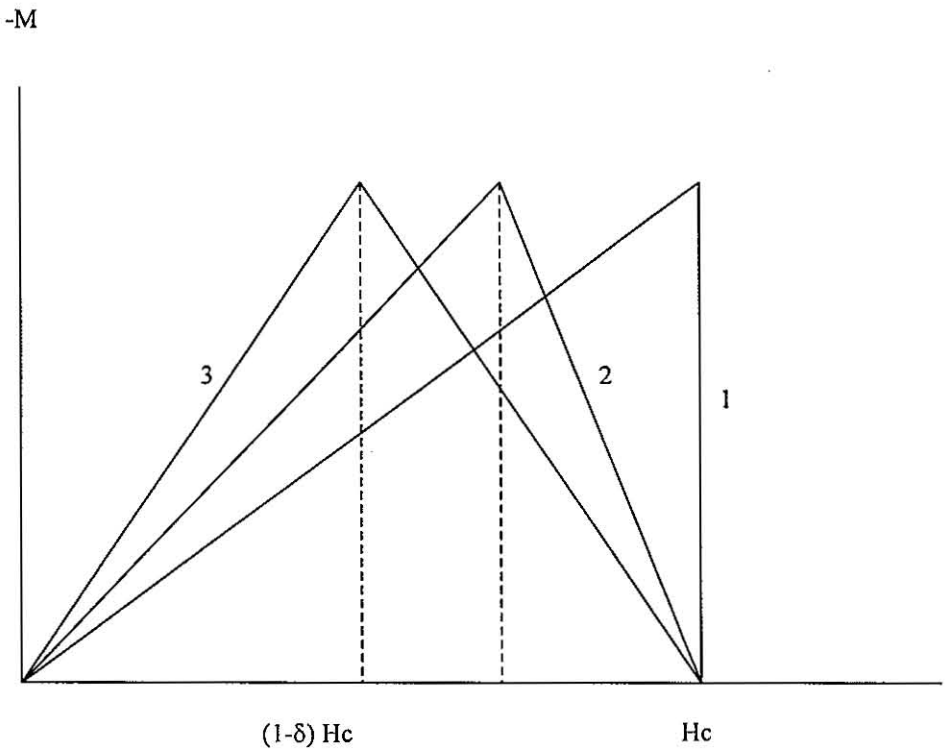

Figure 1.6 Different M vs. H curves of type I superconductor with different demagnetizing factors δ: (1) δ = 0; (2) δ =1/3; (3) δ=1/2

1.2 High T_c Superconductors

High T_c superconductors (HTSC), comprised of various metal oxides mostly involving Cu, are different from conventional type II superconductor. The strong anisotropy along different direction contributes [15] to the complex electrical behavior. From low temperature to high temperature, HTSC will show superconducting, conducting, semiconducting, and insulating behaviors, respectively.

Compounds of light rare earth (LR) family of $LRBa_2Cu_3O_{7-\delta}$ all have T_cs around 90K. They have perovskite structure, which contains Cu-O planes and Cu-O chains (Figure 1.7). LR and BaO layers separated Cu-O planes and chains. Among the oxygen atoms, chain sites (O_1) is the most mobile one, which diffuse easily, leaving oxygen vacancies there. The resultant oxygen vacancies in the chains will cause changes to the crystal structures and result in the changes of magnetic and electronic properties. It is believed that the Cu-O chains works as a charge reservoir, supplies electrons (holes) in the Cu-O planes, which form the Cooper pair and produce the supercurrent. $EuBa_2Cu_3O_{7-\delta}$ is one member of the $REBa_2Cu_3O_{7-\delta}$. It has a high T_c of 93K. According to equation 1.1, it has a very short coherence length. The magnetization of a high T_c superconductor is like that of a typical non-ideal type II conventional superconductor with a reversible magnetization region (Figure 1.8). Typical type II superconductors like $EuBa_2Cu_3O_{7-\delta}$, which have small ξ, are very sensitive to small-scale structural and chemical imperfections. If ξ is more comparable with the lattice parameter defects, it is more effective to pin the vortex.

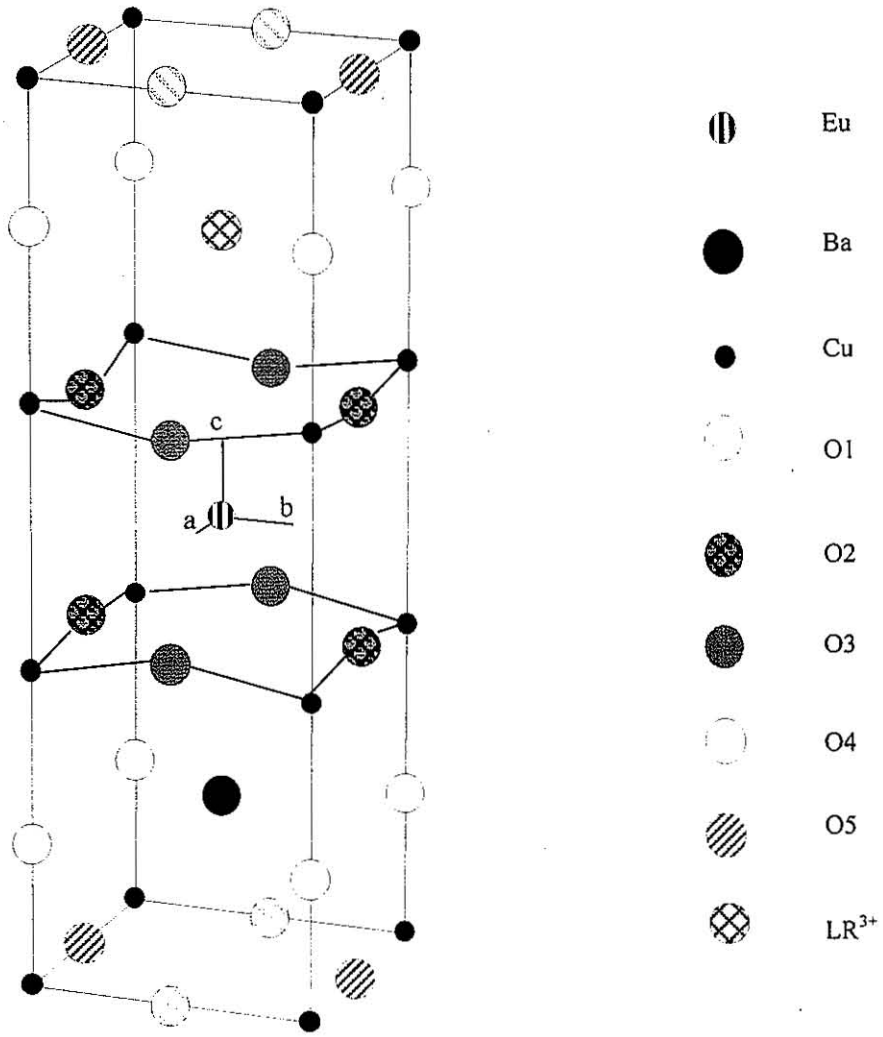

Figure 1.7 Structure of $Eu(Ba_{1-x}LR_x)_2Cu_3O_{7+\delta}$

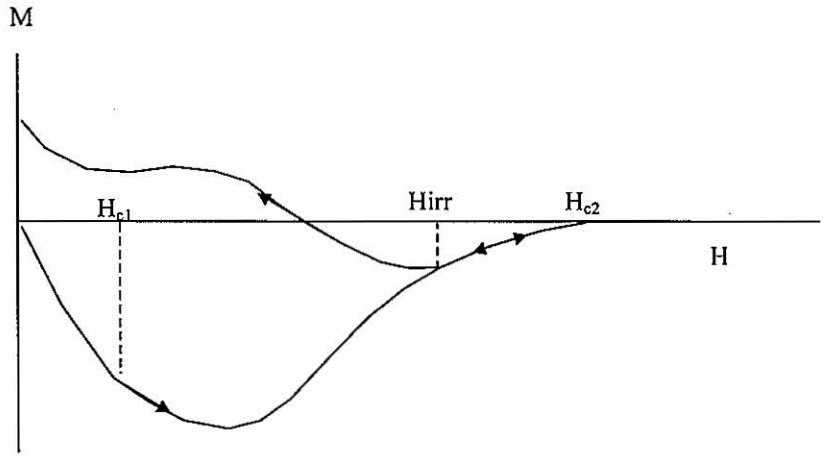

(a)

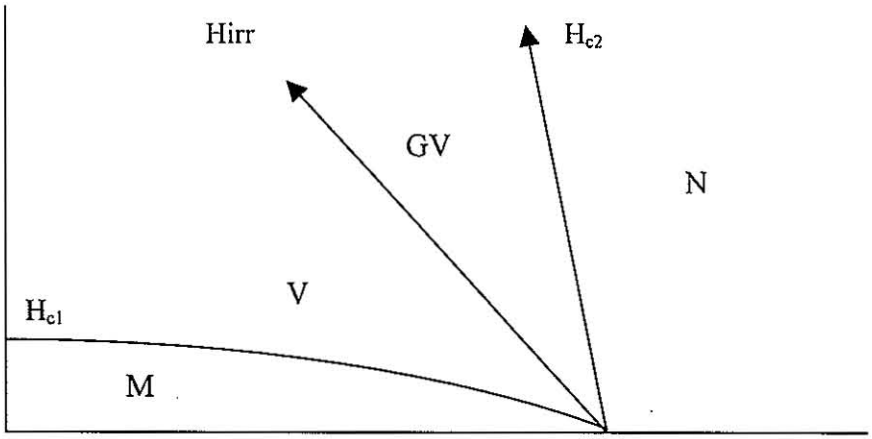

(b)

Figure 1.8 (a) hysteresis of HSTC; (b) the state diagram of HSTC, M for Meissner State, V for Vortex State, GV for glass Vortex State, N for normal state

CHAPTER 2. LITERATURE REVIEW

2.1 Conduction Mechanism of High T_c Superconductors

Considerable research have been devoted to studying Eu $(Ba_{1-x}LR_x)_2Cu_3O_{7+\delta}$ solid solutions (EuLR123ss). The LR elements could be Pr, La, Eu and Nd. These ions can occupy Eu^{3+}(½, ½, ½) or Ba^{2+} (½, ½, z) sites. Here, we only consider the latter case. Since all of the LR^{3+} have smaller radii than Ba^{2+}, small amount of substitution will not change the crystal structure, but it will suppress superconductivity [8-12]. Because the LR^{3+} ion has different valence from Ba^{2+}, charge conservation requires more negative charge carriers-electrons, which occurs by increasing O^{2-}content.

Most of the ceramic high T_c materials are P type, i.e. the superconductivity is dominantly controlled by the hole concentration. For EuLR123ss, the hole concentration can be adjusted by doping Ba sites and adding or reordering the oxygen. For each LR^{3+} substitution, ½ oxygen is needed to balance the charge. A detailed study on $Nd_{1+x}Ba_{2-x}Cu_3O_{7+\delta}$ [16] showed that for all the doping levels, $0.04 \leq x \leq 0.5$, the hole concentration of these fully oxygenated Nd123ss was constant. The holes were transferred from the Cu-O chains to the Cu-O planes. In the fully oxygenated orthorhombic structure, the extra oxygen will occupy the anti-chain (O5) sites. Due to their relative isolation, the O5 does not contribute directly to the superconductivity.

The addition of the oxygen will redistribute the charge in the structure. The

localization of the holes will suppress the superconductivity. With increasing the doping level, the crystal structure changes from orthorhombic to tetragonal. However, the ionic size dependence of the suppression is not a linear relationship. Among them, Pr^{3+} on Ba^{2+} sites behavior abnormally [17]. It suppressed superconductivity at a faster rate than other rare earth element. But the structural distortion caused by it is consistent with other EuLR123ss. One explanation is the suppression caused by Pr is electronic in nature instead of magnetic.

Figure 1.7 shows the structure of Eu $(Ba_{1-x}LR_x)_2Cu_3O_{7+\delta}$. Conventionally, the Cu-O plane is called conduction planes. It is believed that the Cu-O chains works as a charge reservoir. When LR^{3+} is on the Ba^{2+} sites, it will grab an electron from the Cu-O plane and leave a hole there. The holes will form copper pairs to conduct supercurrents. Supercurrent flows in the layered structure formed by Cu-O planes with a single rare earth atom to separate them. Defects in the structure can change the supply of the free electrons and as a consequence, it will change the electron states. Because T_c is a function of the number of charge carriers, the defect will change T_c indirectly.

2.2 Crystal Structures

The stoichiometric Eu123 has an orthorhombic structure. Generally, $a < b < c$ and $b \approx 1/3$ c. With increasing the doping level, more oxygen is needed to balance the charge. The introduced oxygen will go to the O5 sites easily. Therefore, with extra oxygen filling in O5 sites, which is on the a-axis, a-axis will expand gradually. Because site (O1) is very mobile, which is on the b axis, it will also go to O5 at the same time and b axis shrinks gradually. As

a matter of fact, for each LR^{3+}, only ½ oxygen is required. Local charge balance can be maintained by adjustment on O1 and O5 [18]. When the doping level is large enough, eventually, the probability of oxygen occupying the O5 is the same as that of Occupying O1. Then the structure becomes tetragonal. Also, because of the smaller sizes of the substitution ions than that of Ba^{2+}, the c axis will decrease gradually as well as the volume.

Xu et. al. [17] systematically studied the EuLR123ss, LR = La, Pr, and Eu. Figure 2.1 shows how the lattice parameters change with the doping level. With more light rare-earth elements substituting the Ba^{2+}, a- axis becomes larger and b axis becomes smaller. Eventually, EuEu123ss changes from orthorhombic to tetragonal at $x \approx 0.11$, EuPr123ss does at $x \approx 0.13$ and EuLa123ss at $x \approx 0.15$. The a-axis of the tetragonal structure begins to decrease due to the smaller size of the substituting ions. In terms of ion size, $Eu^{3+} < Pr^{3+} < La^{3+}$, so it is not hard to understand that Eu suppresses the lattice parameters at the fastest rate, and La does at the slowest rate. The reason also holds for the trends of c axis and volume.

2.3 Important Characteristics

2.3.1 Critical transition temperature (T_c)

Superconductor behaves as a "perfect" conductor below T_c. However, when the temperature is approaching T_c, the resistivity increased rapidly within a very small temperature interval. Above T_c, the superconductivity is destroyed and the superconductor enters the normal state. Therefore T_c is a very important characteristic of superconductors. As mentioned above, T_c is influenced by the number of free charge carries (N_0).

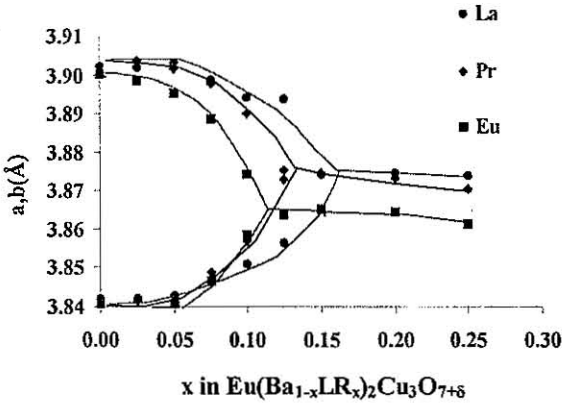

(a)

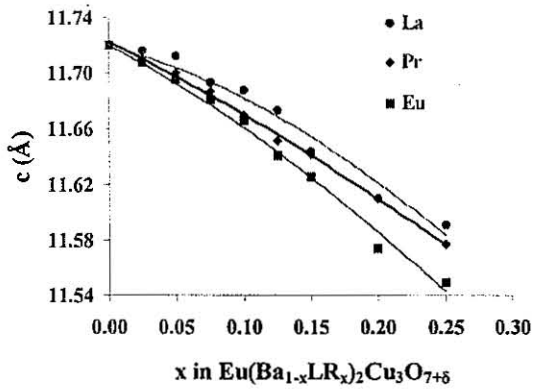

(b)

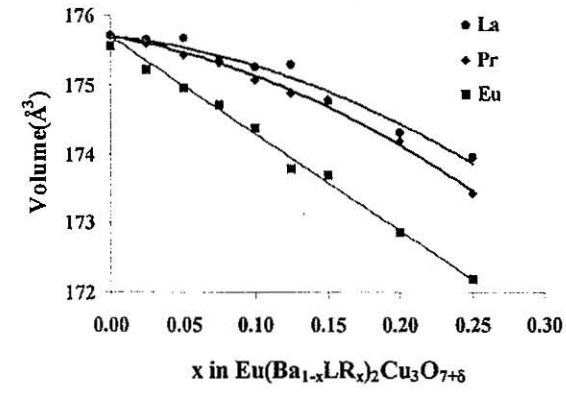

(c)

Figure 2.2 The lattice parameters with the different dopants and doping levels: (a) a, b axes; (b) c axis; (c) volume

Equation 2.1 gives the relationship between T_c and N_0.

$$T_c \propto \exp\left(-\frac{1}{N_0 V}\right) \qquad \text{equ. (2.1)}$$

EuLR123ss is P-type superconductor. If LR substitutes Ba, grab an electron, the hole will be localized and the number of free holes is reduced. By using equation (2.1), it is obvious that the heavier the doping level, the lower the T_c. The T_c data of some EuLR123ss are shown in Figure 2.2. It is clear that increasing Pr is similar to the other LR elements in terms of lattice parameter distortion but abnormally in terms of T_c depression. Its T_c vs. x is below that of EuEu123ss instead of between those of EuEu123ss and EuLa123ss as expected based on ionic size. The suppression of T_c of Eu and La doped sample could be explained in magnetic behavior. Abriskosov [19] explained that the Cooper pairs were formed by electron-phonon interactions. Each particle of a pairs has the same magnitude but opposite momentum. If the pair strike on a nonmagnetic impurity, the scattering pattern will not change and the particles keep anti-parallel. If the pair contacts a magnetic impurity, then scattering will be different for each particle, suppressing T_c quickly. In regard to EuPr123ss, there is still no agreement on the current theories about the nature of the suppression [17,20-23].

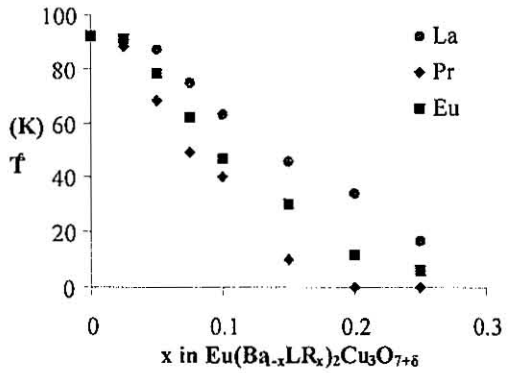

Figure 2.2 The transition temperature for superconductors with different dopants and doping levels.

2.3.2 Critical current density (J_c)

A current flowing in a superconductor will generate a magnetic field. Figure 2.3 shows the relationship between H and I. The specimen is a long superconductor wire. Usually, current density is a better parameter than current, because of its independence of the cross-section area of the sample. According to Ampere's law, the magnetic field generated at the surface of a wire was shown in Equation (2.2):

$$H = \frac{2I}{cr} \qquad \text{equ. (2.2)}$$

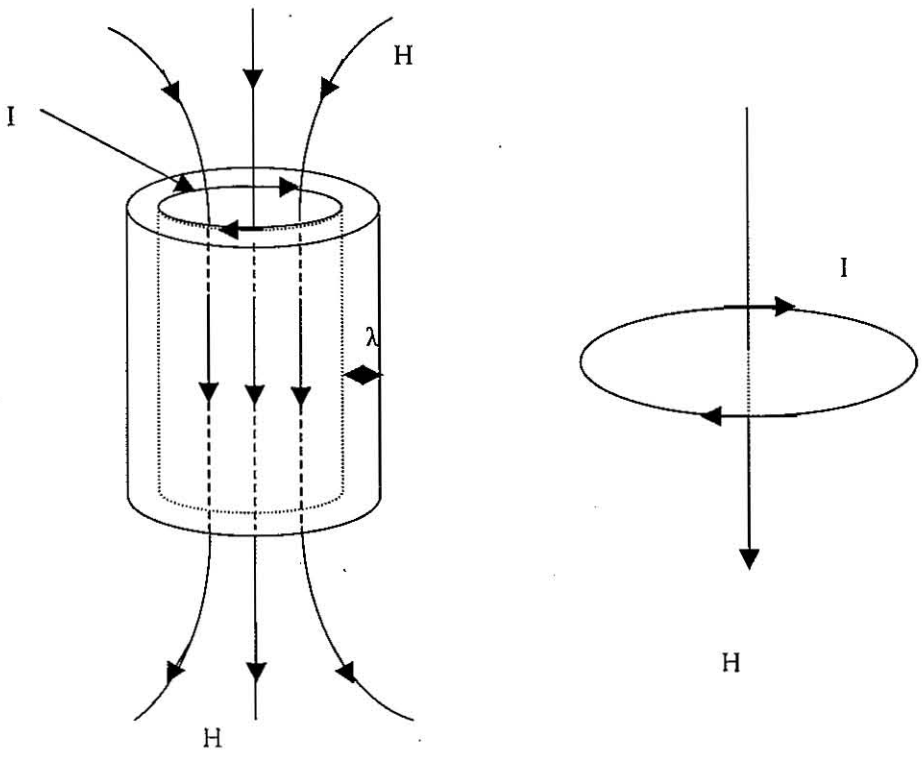

Figure 2.3 Magnetic field generated by a circulating current in a wire within skin depth of λ

Here, c is the light speed and r is the radius of the wire. If the supercurrent keeps increasing, then the generated magnetic field also increases. Because of the Meissner effect, the specimen will expel the magnetic flux. However, when the applied field reaches a critical value, certain amount of supercurrent was produced and consequently, self - generated field will destroy the superconductivity. This critical current density is denoted as J_c and the corresponding applied filed is H_c. Silbee's rule explained such phenomenon and it applies for type I superconductors [8-12,15]. Assume the supercurrent flows within the depth of λ from the skin of the wire, then the total cross-section area that the current flows is $A = 2\pi r\lambda$. Therefore the flowing current is:

$$I = AJ = 2\pi r\lambda J \qquad \text{equ. (2.3)}$$

Insert equation (2.3) back into equation (2.2), which gives

$$H = 4\pi\lambda\frac{J}{c} \qquad \text{equ. (2.4)}$$

If $H = H_c$,

$$J = J_c = \frac{H_c}{4\pi\lambda} \qquad \text{equ. (2.5)}$$

Equation (2.5) just gives us a rough estimation of J_c as a function of H_c.

Later, GL theory gives a more precise calculation of J_c. According to this theory, the free energy can be expressed in terms of the order parameter. For the normal to superconductor phase transition, the order parameter is a wave function of the superconductor state Ψ. By deriving the GL equation, the free energy was minimized at some critical values, which determined the J_c (equation (2.6)).

$$J_c = \frac{cH_c(t)}{3\sqrt{6}\pi\lambda(t)} \propto (1\text{-}t)^{3/2} \qquad \text{equ. (2.6)}$$

This equation gives the theoretical value of J_c when t is close to T_c.

Bean model established equations that are used to describe the relationship between critical current and applied field. Maxwell equation $\nabla \times B = 4\pi \frac{J_c}{c}$ relates J_c to the magnetization M. Assume a specimen is a slab with a width of d. After the magnetic field fully penetrate the slab, the width of the hysteresis loop is proportional to J_c

$$J_c \propto 2\frac{\Delta M}{d} \qquad \text{equ. (2.7)}$$

This inductive measurement of J_c is widely used for conventional superconductors and HTSC. In fact, ΔM varies with field for most samples, i.e. J_c is a function of the field [Figure 2.4].

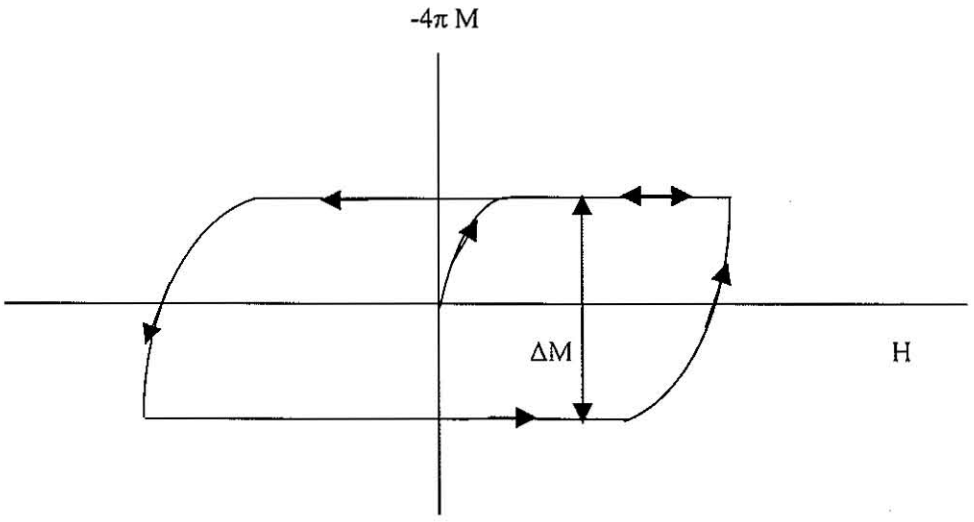

Figure 2.4 Hysteresis loop for calculating critical current density J_c in Bean critical state model

Assuming the z-axis is along to the axis of a wire, in order to satisfy the Maxwell equation, the induced magnetization B only has a θ component. Because of the symmetry of the wire, B (θ) is constant and the current density (J) is along Z direction only [11]. According to Bean Model, the distributions of J (J_z) and B (θ) are illustrated in Figure 2.5. It is clear that the magnetization lineally decreases to zero from the skin to the inner part of the specimen. However, J is constant in the bulk, then drops to zero abruptly at the depth of λ. Whenever the flowing current changes, the current density will jump to the new value suddenly.

In real material, especially in the vortex-state of type II superconductor, there exist vortices. Each vortex carries a magnetic flux Φ_0. Because of the interaction of magnetic field and the electric field, the vortex will feel the electrical field generated by the applied magnetic field. The vortex flux line interacts with the electrical field, according to equation (2.8), a force will act on the vortex and cause the vortex to move.

$$F = J \times B \qquad \text{equ. (2.8)}$$

By using Faraday's Law, we know that the motion of the flux will produce an electrical field:

$$E = B \times V. \qquad \text{equ. (2.9)}$$

This electric field is along the direction of the supercurrent, which helps to increase J. Therefore, when J approaches J_c, the J component generated directly by the applied field is far below J_c. Energy dissipation from the vortex motion is another consideration. In order to get high J_c, vortex motion has to be prevented. Introducing defects to pin vortices is a commonly used method.

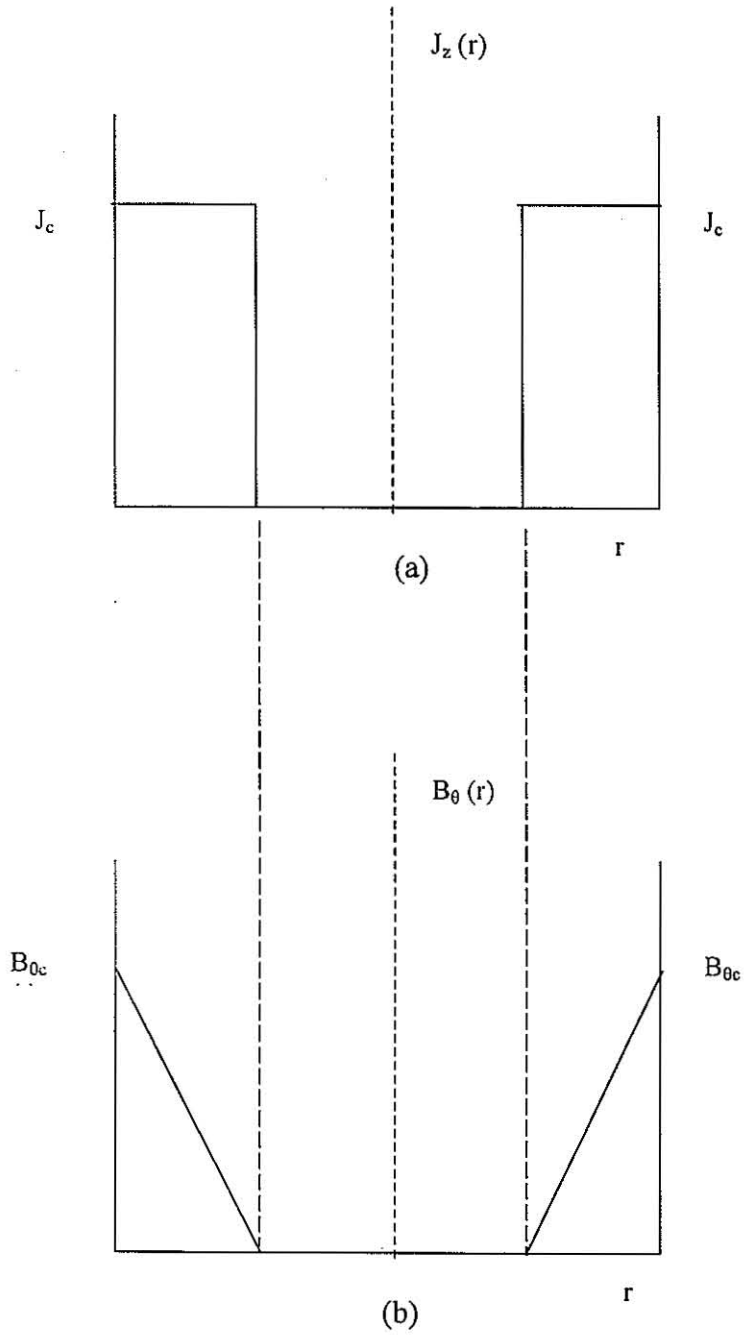

Figure 2.5 (a) the critical current density J; (b) magnetic field B_θ distribution according to Bean critical state model

The hysteresis loop of single crystal of Y123 has a fishtail [24,25]. EuLR123 has similar shape of hysteresis loop, which is plotted in Figure 2.6. There are several models, which explained the fishtail features [26]. For all of the models, J increases as the applied field increases till it reaches a peak value and then decrease at higher field due to the collapse of the global order parameters [27]. Therefore J_c is a function of not only field and temperature but also compositions and defect structure.

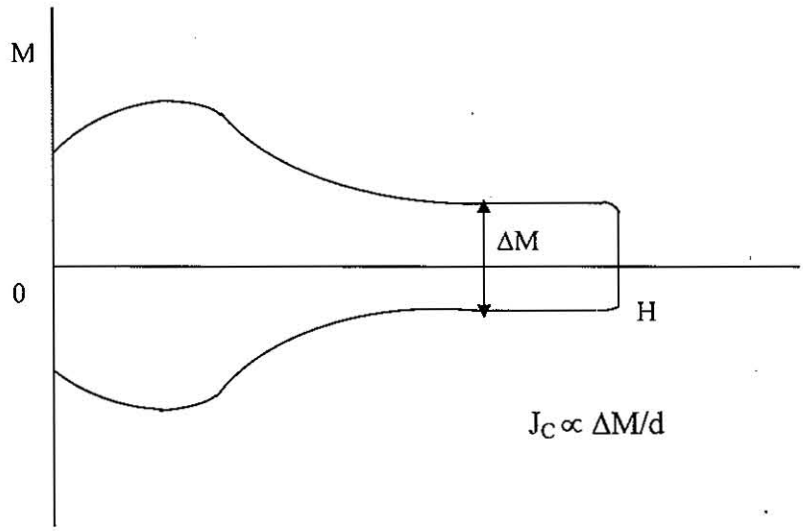

Figure 2.6 The fishtail feature of hysteresis loops of some superconductors

2.3.3 Upper critical field (H_{c2})

H_{c2} is specific to type II superconductor. Since J_c is related to flux pinning and scales with H_c, determining H_{c2} is another way to study the flux pinning. Hao-Clem Model [28] allows for the accurate determination of H_{c2} for type II superconductor in the reversible magnetic region. Because of EuLR123ss strong anisotropy along different direction, the H_{c2} along the c axis must be different from that along the a-b plane. Research done on Y124 by Ming Xu [29] indicated that the H_c for H || c and H || a-b is the same, but GL parameter κ is much different, resulting different H_{c2} for these orientations.

2.4 Vortex Flux Pinning

2.4.1 Vortex state

For type II superconductors, there is a special state between Meissner state and normal state, which is vortex-state. Because of the surface energy of the interface between normal and superconducting regions is negative, the system favors more borders between the normal and superconducting zones. In equilibrium status, the system will be the mixture of normal and superconducting regions. The vortex forms as normal cylindrical regions with supercurrents circulating outside to shield the magnetic field. When applied field approaches H_{c1}, the first flux line enters into the superconductor. At first, for each vortex, the radius of the cylinder is roughly the same as the coherence length ξ, and the spacing between two vortices is close to the penetration depth λ due to mutual repulsion. Since the vortices interact, they will be ordered in a regular way, which is called Abrikosov lattice. With the increasing of H, the spacing between flux vortices becomes shorter and shorter and then forces the flux line spacing to approach ξ and reduce the critical current. Figure 2.7 shows the picture of the change of spacing under different conditions. When the flux lines spacing equals ξ, then the superconductivity is lost.

According to equation (2.8), the vortex will be displaced by forces generated by the interaction of electrical and magnetic fields. However, defects like grain boundaries, dislocations and point defects in the specimen can impede the vortex motion. For conventional type II superconductors, the vortex lattice is very rigid usually when $T << T_c$

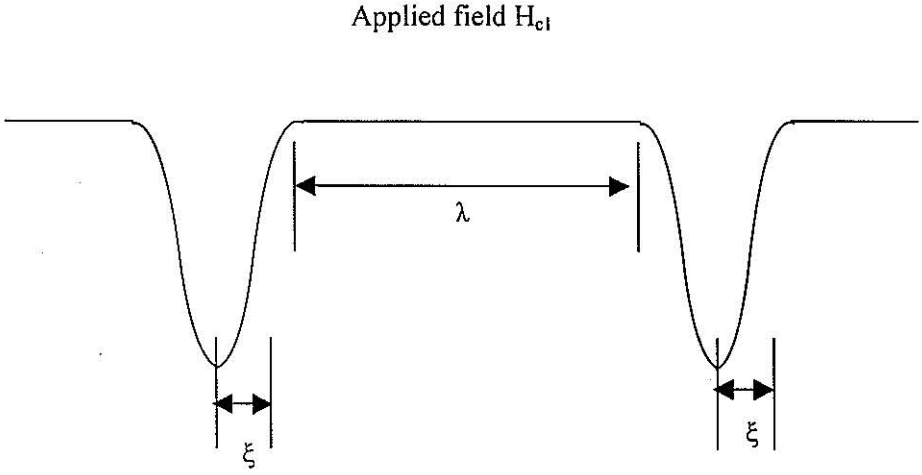

(a)

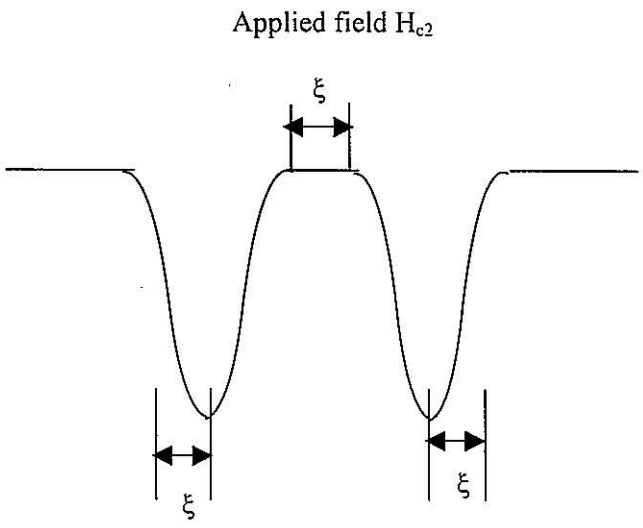

(b)

Figure 2.7 The radius of vortex and vortex spacing (a) applied field is H_{c1}; (b) applied field is H_{c2}

and $H < H_{c1}$. One flux line can not move independently. If we just want to move one flux line, then we need enough energy to move the whole flux lattice together. For HTSC, the vortex lattice is softer. Individual flux line can be moved around without affecting other flux lines below H_{irr} [30]. Some research [31] showed that the vortex of LTSC (low Tc superconductors) is cylindrical. However, for HTSC, the vortex is pancake-like because of its extreme anisotropy. Along different directions, the spacing between vortices varies a lot.

Usually, below the critical field that indicates the irreversible to reversible transition (H_{irr}), flux pinning take places and a supercurrent flows. Below H_{c2} but above H_{irr}, the energy is dissipated by freely moving unpinned flux lines. For LTSC, H_{irr} is very close to H_{c2}. For HTSC, H_{irr} is much smaller than H_{c2}. Similar to the melting point of a glass, flux lattice also has a "melting" point. T_m is denoted as this special temperature. In case of HTSC, $T_c > T_m$. When temperature is between T_c and T_m, the flux can move freely. Thus, HSTC has one more sub-vortex state–vortex glass state. In this state, the magnetization is reversible.

Flux melting could be defined as a status when the average of random excursion of flux exceeds the lattice spacing about 20%. Two ways can be used to melt flux lattice. One is to increase the random excursion distance by increasing the temperature. Another one is to reduce the lattice spacing by increasing the applied field [32].

Because of the existence of Cu-O layer, pancake vortices are coupled together along the c-axis. This made the reversible transition in a magnetic field broader [33].

2.4.2 Flux pinning

Because J_c is a reflection of resistance to vortex motion, one way to improve J_c is to pin the flux vortices. Since pinning is only effective for defect whose size is $< \xi$, only pinning

caused by impurities will be discussed. For our system EuLR123ss, the impurity is the excess LR elements on the Ba sites. Figure 2.8 illustrates a pinned and an unpinned vortex. Figure 2.8b is the energy density distribution around the vortex. At the center of the vortex, the free energy density is zero and it increases with the increasing of distance to the center. Eventually, it will saturate and approach a maximum value of E_s. Assume there is an impurity inside of the vortex, which has a volume of V. Then the total energy of this system $E = E_v + E_{imp}$. Here, v is for vortex, imp is for impurity, $E_{imp} = \int_0^V E(r)dv$. If the vortex moves, leaving the impurity out of it, the total energy will be $E' = E'_v + E'_{imp}$. Here, $E'_{imp} = E_s^* V$. Because E(r) is always less than E_s, E is always less than E'. So the system with E will be more stable than that with E'.

The impurity size also plays role in pinning effeteness. Assuming the impurity is large compared to the size of the radius of the vortex, then the vortex has some freedom to move around without leaving the potential well. If the defect is on the size of ξ, it has less freedom to move and dissipate less energy. In this instance, the enhancement of J_c is more effective. Therefore, an impurity with size comparable to vortex is preferred.

2.5 Summary

Studies on the $Eu(Ba_{1-x}LR_x)_2Cu_3O_{7+\delta}$ families with Pr, Eu, La doping on the Ba sites have been conducted. However, $Eu(Ba_{1-x}Nd_x)_2Cu_3O_{7+\delta}$ has not yet been studied systematically.

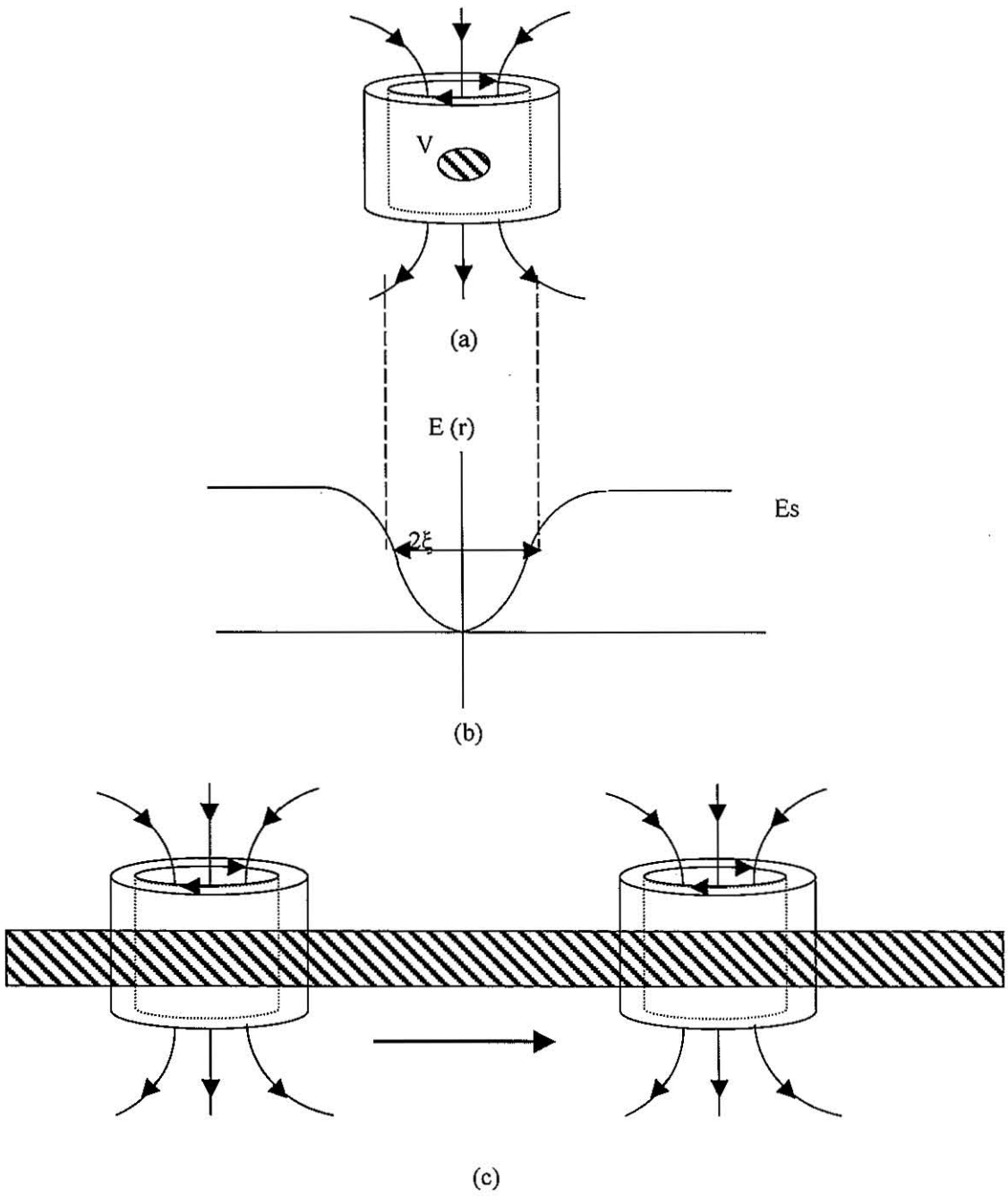

Figure 2.8 (a) single vortex with small size impurity inside, which has volume V; (b) the energy distribution along the radius; (c) a vortex with long impurity pass through it has some free moving space.

In the periodic table, the atomic number of Nd is between those of Pr and Eu. Correspondingly, the Nd ion size is between those of Pr and Eu ion sizes too. One interesting topic is whether Nd series has similar trend in terms of the lattice parameters, magnetic properties and etc.

It is well known that a small impurity helps to pin flux. In order to investigate the dependence of doping level, sample is lightly doped where the T_c is depressed a little. Because of the J_c and H_{c2} are closely related to flux pinning, they are good methods to study flux pinning in two different ways. However, H_{c2} is very hard to be characterized. One alternative way is to investigate the corresponding M vs. H and M vs. T curves to see how they depends on the dopants and doping levels. Also, the methods to correct the background of the curves itself are worth studying.

CHAPTER 3. METHODS

3.1 Materials Preparation

EuLR123ss powders were prepared with solid state reaction, which is comprised of grinding the oxides and carbonates, calcination to remove the CO_2 and sintering to reaact the final products. High purity powders of Eu_2O_3, $BaCO_3$, CuO and Pr_6O_{11}, Nd_2O_3, La_2O_3 were dried in static air for more than 48 hours at 1000°C, 700°C, 550°C, 1000°C, 950°C, 750°C, respectively. The dried powders were then cooled down in a dry-box filled with Nitrogen. Agate mortar and pestle were used to grind the dried powders to fine particles, and then stored in a N_2 glove box for later use. The amount of carbonates and oxides in each sample is listed in Table 3-1.

A motorized agate mortar and pestle were used to grind and mix the approximate 10 gramms of powders for each sample to sub-micron particale size for about 12 minutes under nitrogen. Such procedure was repeated several times till the power looks homogeneously distributed. After this step, powder was pressed at 6.89×10^7 Pascal to make a pellet with diameter of 2.54. The pellets were calcined on MgO single crystal wafer in forced air furnace with a mixture of 80% N_2 and 20% O_2 flow of about 10 l/m and the CO_2 was removed. The pellets were heated at 880°C for 24 hours. Differential Thermal Analyzer (DTA) was used to determine if the sample is phase pure below 880°C. Generally, the sample for DTA analysis was heated in 100% oxygen from 600°C to 1150°C at the rate of 10°C/min.

Table 3-1 The compositions of $Eu(Ba_{1-x}LR_x)_2Cu_3O_{7+\delta}$

Sample ID	Composition	Eu_2O_3 (g)	Ba_2CO_3(g)	CuO (g)	Others oxide(g)	Total (g)
LG25	$EuBa_2Cu_3O_{7-\delta}$	4.349	9.754	5.898		20
LG26	$Eu(Ba_{.975}La_{.025})_2Cu_3O_{7+\delta}$	2.179	4.765	2.955	La_2O_3 0.101	10
LG27	$Eu(Ba_{.95}La_{.05})_2Cu_3O_{7+\delta}$	2.184	4.653	2.961	La_2O_3 0.202	10
LG28	$Eu(Ba_{.95}Pr_{.05})_2Cu_3O_{7+\delta}$	2.182	4.649	2.959	Pr_6O_{11} 0.211	10
LG29	$Eu(Ba_{.975}Pr_{.025})_2Cu_3O_{7+\delta}$	2.178	4.763	2.954	Pr_6O_{11} 0.105	10
LG30	$Eu(Ba_{.975}Eu_{.025})_2Cu_3O_{7+\delta}$	2.286	4.761	2.953		10
LG31	$Eu(Ba_{.95}Eu_{.05})_2Cu_3O_{7+\delta}$	2.398	4.645	2.957		10
SG24	$Eu(Ba_{.975}Nd_{.025})_2Cu_3O_{7+\delta}$	4.356	9.527	5.908	Nd_2O_3 0.208	20
SG25	$Eu(Ba_{.95}Nd_{.05})_2Cu_3O_{7+\delta}$	4.364	9.300	5.919	Nd_2O_3 0.417	20
SG26	$Eu(Ba_{.925}Nd_{.075})_2Cu_3O_{7+\delta}$	4.372	9.071	5.930	Nd_2O_3 0.627	20
SG27	$Eu(Ba_{.9}La_{.1})_2Cu_3O_{7+\delta}$	4.380	8.842	5.940	Nd_2O_3 0.838	20
SG28	$Eu(Ba_{.85}La_{.15})_2Cu_3O_{7+\delta}$	4.396	8.381	5.962	Nd_2O_3 1.261	20
SG29	$Eu(Ba_{.8}La_{.2})_2Cu_3O_{7+\delta}$	4.412	7.917	5.984	Nd_2O_3 1.687	20
SG30	$Eu(Ba_{.75}La_{.25})_2Cu_3O_{7+\delta}$	4.428	7.449	6.006	Nd_2O_3 2.117	20

If the samples are not phase-pure, they are reground, pressed into pellets and calcined in dry air again. The purpose of this step is to remove all the carbon as CO_2.

After successful calcination, the samples are annealed. The ground powder is pressed into a pellet, annealed in 100% oxygen with a flow rate of 20 l/m. Multiple annealings and regrindings are typically required to make phase-pure materials. Each sample is to be heated about 20°C below its first melting temperature for 24 or 48 hours. The sample is checked with DTA after each step. However, for a few samples, a tiny amount of a second phase couldn't be removed by multiple annealings.

The final step is to oxygenate the sample. The combined temperature profile used for sinter and oxygenation is described in Figure 3.1. The sample was first heated up to 950°C at the rate of 10°C/m, and then soak oxygen for 48 hours. After that it was furnace-cooled to 550°C ~ 450°C to be fully oxygenated for 24 hours and then furnace-cooled to room temperature. To obtain powders within the same size range, the sample had to be heat treated again, because the grain size is process-dependent. Since the peritectic decomposition temperature is compositionally dependent, the process temperature should be decided according to the previous DTA result. Optical Microscope was used to determine the grains size. In our experiment, the grain sizes of the EuLR123ss except EuNd123ss are about 45~60μm. The grain size of EuNd123 is about 10~20 μm even after long time annealing. Eventually, the sample was ground to powder and sift to get particle size around 25~38 μm.

To insure the sample is fully oxygenated, a 2nd oxygenation separated from annealing was done on ground powders. The sieved powder has a larger surface area to volume ratio for oxygen than the corresponding pellet, which decreases the diffusion distance. In order to prevent the silicon or other impurities to fall in the fine powder, a crucible containing the

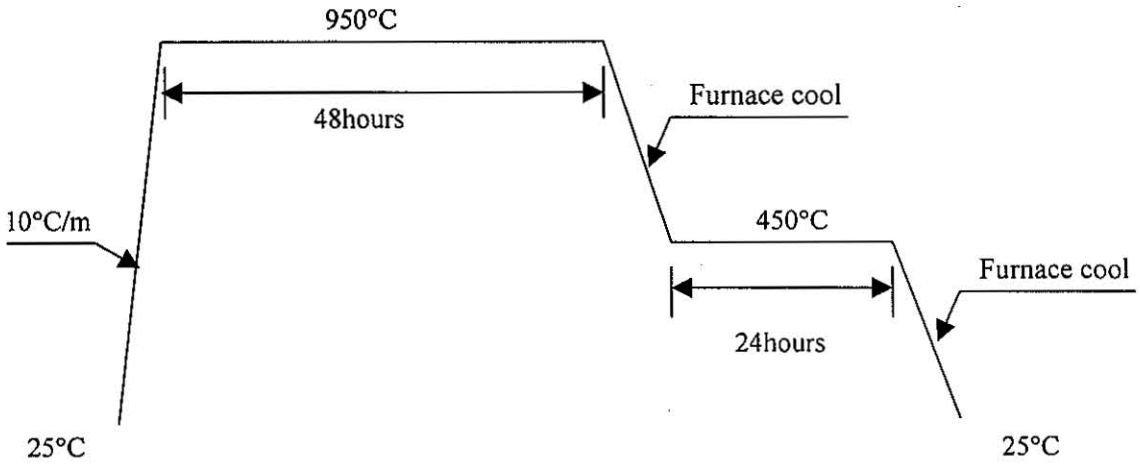

Figure 3.1 The temperature profiles for processing samples

powder was covered by a gold sheet.(Figure 3.2b).

Hao-Clem model that is used to fit magnetization measurement to determine H_{c2} requires that the sample should be single crystal or grain-aligned. Using an applied magnetic field can align single grain powders. As a test, $EuBa_2Cu_3O_{7-\delta}$ powder with particle size less than 25 μm was mixed with epoxy and then daubed on a glass slide (Figure 3.3). A 9 Tesla field was applied vertically to the sample plane for about a half-hour giving the grains inside of the epoxy have enough time to align with the applied field. Then the sample was heated to let the epoxy cured to fix grains. X-ray diffraction analysis was done on this sample to check the alignment condition (Figure 3.4a). Obviously, all of the (*0 0 l*) peaks are depressed and all the (*h k 0*) peaks are enhanced.

This demonstrated that the a-b planes are aligned in the direction of the applied field with the c-axes randomly distributed in the plane of the glass slide.

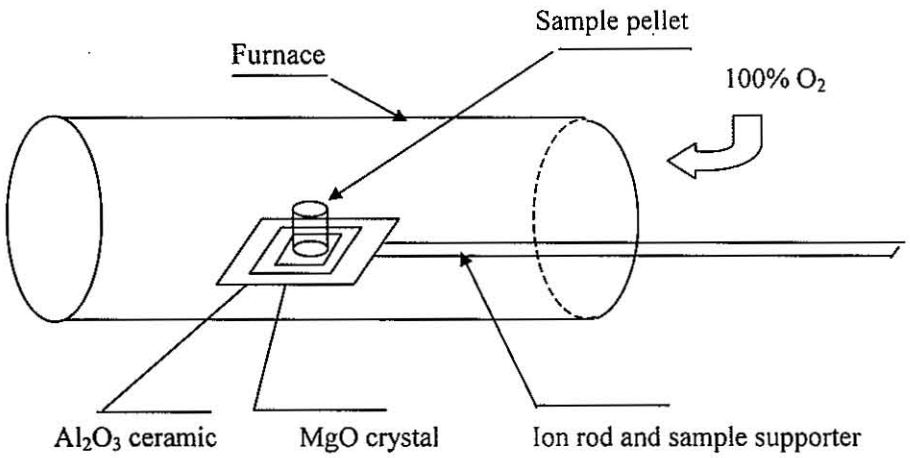

(a)

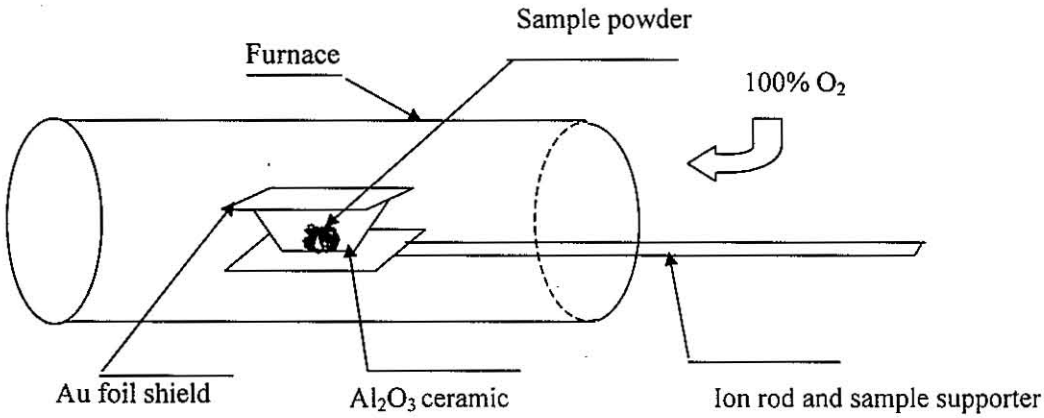

(b)

Figure 3.2 The setup of furnace (a) for annealing (b) for oxygenation

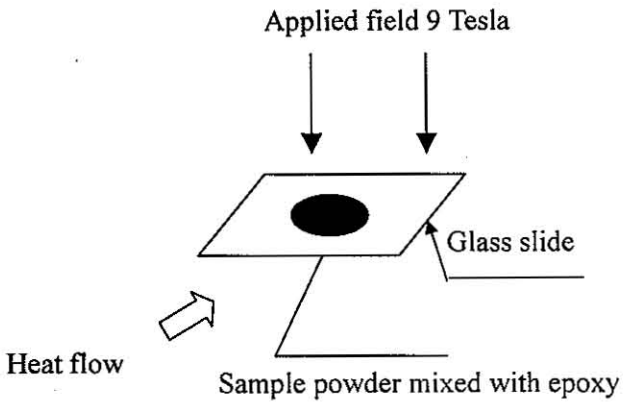

Figure 3.3 The setup for sample alignment with field ⊥ glass slide

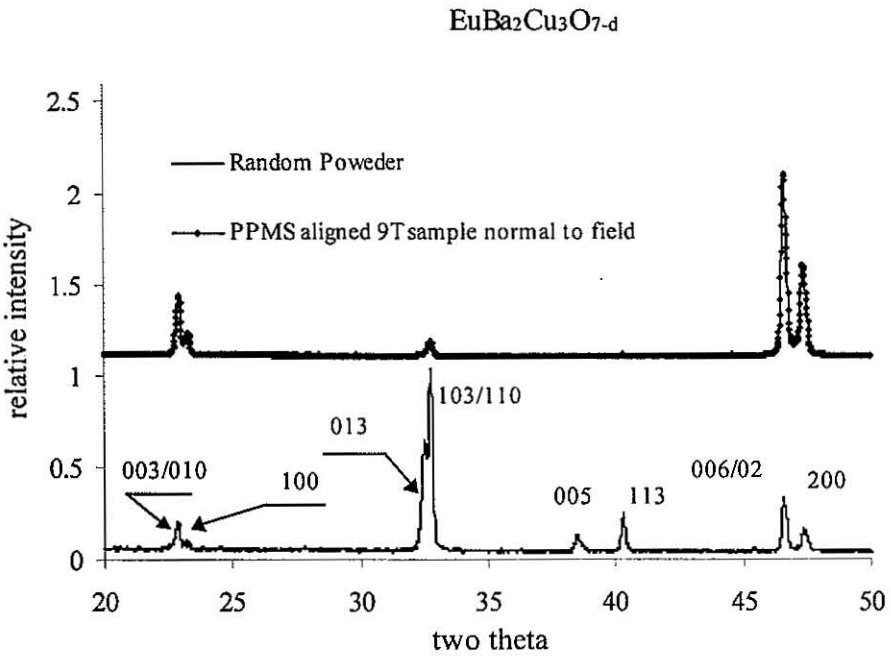

Figure 3.4 X-ray patterns for random powder and a-b plane aligned sample

In order to align the c-axis orthogonal to the glass slide, the sample is rotated with the rotation axis perpendicular to the field (Figure 3.5). Because of the limitation of the equipment, the applied field is only about 2 T. The field is parallel with the sample plane but normal to the rotation axis.. The rotation rate of the sample is about 15 r/m. After rotation for about 1 hour, an electrical heat gun was used to speed up the curing process. XRD of the sample confirms the c-axis is aligned (Figure 3.6).

Because of the uncertainty of the loading fraction of the epoxy, the glass slide is not an ideal sample holder. Instead a copper cube with a hole cylindrical is used to contain the powder epoxy mix. The dimension of the cube is about 4 mm and the diameter of the hole is about 3 mm. An Al foil is attached to the bottom of the cube with Permabond Industrial Grade 910 glue to make a cup. About 20 mg of sieved powder with particle size less 25 μm and epoxy was put in the cup. The powder is aligned so that c axis is parallel to the hole as mentioned above. Because of the difficulty to do x-ray analysis, optical microscopy was used to observe the surface of the sample to check the alignment condition.

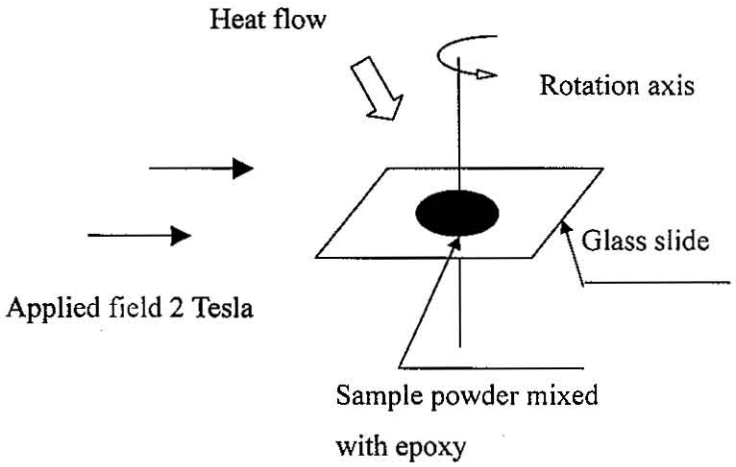

Figure 3.5 The setup for sample alignment with field || glass slide

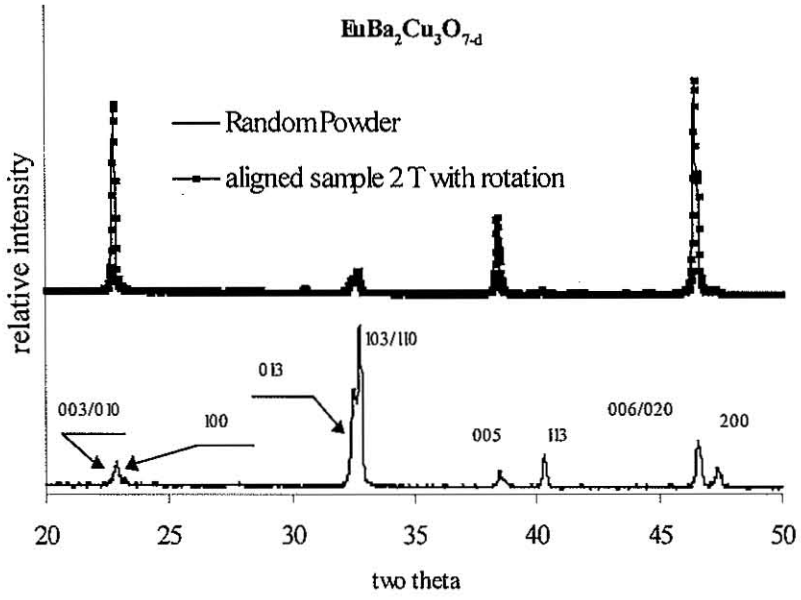

Figure 3.6 X-ray patterns for random powder and c axis aligned sample

3.2 Characterization

3.2.1 Differential thermal analysis (DTA)

The DTA used in these experiments is a Model DTA 7 produced by Perkin Elmer. Typical sample for DTA is 30~50 mg of powder. In order to simulate the processing environment, 100% oxygen is used as the atmosphere. The measured temperature range is typically from 600°C to 1150°C with a heating rate of 10°C/m.

3.2.2 X-ray diffraction (XRD)

The x-ray diffractmeter used is s Philips PW1830. The samples for x-ray analysis are powders ground and sieved to lower than 50 μm. The powder is adhered to a glass holder

with the help of vacuum grease.

XRD is used to check the phase purity, orthorhombicity and lattice parameters of the sample. In order to precisely determine the lattice parameters, a structural refinement processing software: General Structure Analysis System (GSAS) was used.

GSAS consists of several programs, which is for the processing and analysis of diffraction data obtained with x-ray or neutrons for both single crystal and powder samples. For this project, the background contribution was fitted with a cosine Fourier series with a leading constant term background function, which takes the thermal diffuse scattering at high two-theta and the air scattering at low-theta into account. Least square calculation was used to fit the profile peak shape. The profile function used is a combination of Gaussian and Lorentzian terms. $\chi^2 \leq 2$ ensures a good fitting where the residual parameters wR_p and R_p are minimized. The diffractometer's zero offset was characterized by a standard silicon sample. Generally, we fit the coefficient one by one and turn on all of them and fit them together till they are stable. The other parameters like background, lattice parameters etc. are always on.

In our case, some compositions of EuLR123ss are around the O/T transition range. We have to assume they may have either of the structures and fit them. The result with smaller χ^2 and residual parameters was chosen.

3.2.3 Magnetic properties

3.2.3.1 DC SQUID (Superconducting QUantum Interference Device)

All of the magnetization data were obtained by a DC magnetometer, MPMS (Magnetic Property Measurements System) made by Quantum Design. The temperature range is from 2K to 400 K. The accuracy is about 0.5% of the set point. The superconducting magnets constructed from niobium compound can generate the magnetic

field up to 5 Tesla with the error less than 1G [15].

The DC SQUID has four different superconducting components: (1) SQUID; (2) a superconducting detection coil that couples inductively to the sample; (3) a superconducting magnetic shield; (4) a superconducting magnet to generate the large magnetic field.

SQUID is the most sensitive device available for measuring magnetic signal. It does detect B, then puts a small current through a loop to cancel B, thus it is operated as a null detector. With the assistance of Josephson junction, the sensitivity is as low as 10^{-6} emu [15]. The detection coil is composed of a superconducting wire configured in quadruple (Figure 3.7). This configuration reduces the noise produced by the large applied field from the superconducting magnet. A superconducting shield is used to shield the magnetic field generated by the superconducting magnet and any ambient laboratory magnetic fields [34].

The design of the SQUID detection coils is such that a long uniform tube which passed entirely through the coils does not contribute to the measurement signal, which minimize the contribution of sample holder. This contribution is important only for small value of the sample magnetization. Initially, a 15-cm plastic straw (Figure 3.7) was used. However during the measurement, the end of the straw approached the end of the coil set, resulting in significant error where the sample magnetization passed through zero, this error was significantly reduced by using a longer sample holder (Figure 3.8).

3.2.3.2 Characterization of critical transition temperature

T_c is affected by composition, grain size and homogeneity. For our specific EuLR123ss samples, the higher the doping level is, the lower the T_c is. When the doping level increase, T_c approaches zero. For the identical composition but different grain size, the

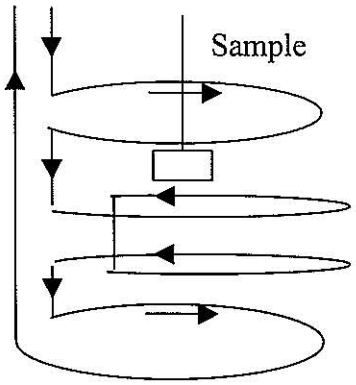

Figure 3.7 The supercurrent flowing in the superconducting detection coil

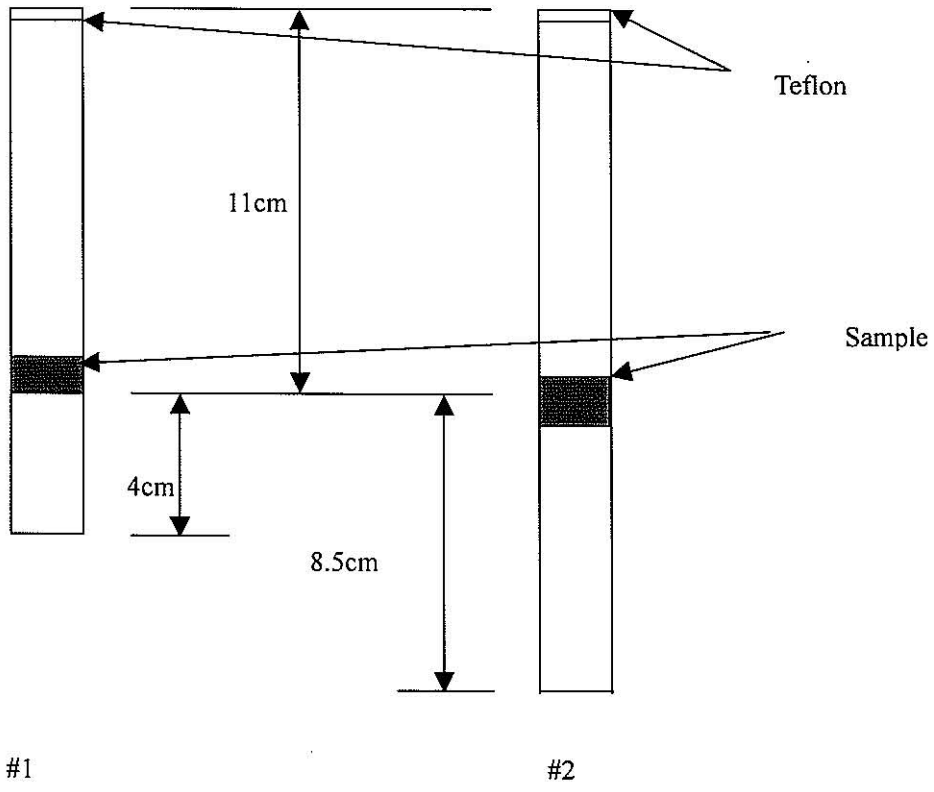

Figure 3.8 Two different sample holders used for magnetization measurements

smaller the grain size, the broader the transition. The homogeneity also affects the transition temperature. If the composition varies subtly, then the local T_c also varies. As a result, the M vs. T curve shows a broad transition region. In this experiment, the sample was first cooled in zero field and then 10 Oe field was applied and data was taken while heating the sample. Once the temperature reached 120K, the sample was cooled back down and the data was taken during the cooling. The absolute value of T_c is also influenced by oxygen content. If the oxygen is removed from the sample, then it is no longer a superconductor. For the partially oxygenated sample, the T_c is reduced [35]. In order to determine the effect of the dopants on T_c, the sample must be fully oxygenated and chemically homogeneous.

3.2.3.3 Characterization of critical current density

Critical Current density is influenced by defects in EuLR123ss. For this specific study, 9 samples were prepared. One is $EuBa_2Cu_3O_{7-\delta}$, the others are EuLR123ss, LR= La, Pr, Eu, Nd, x = 0.025, 0.05. As mentioned in equation (2.7), J_c is inversely proportional to grain size. In this experiment, for easy comparison, we must make sure all the samples have the same particle sizes vary from 25~38 μm. For EuNd123ss, the grain size is about 10~20 μm. For the measurements of hysteresis loop, the temperatures were fixed at 10K, 20K, 50K and 77K, respectively. At each fixed temperature, the applied field was increased from 0 to 5T.

3.2.3.4 Characterization of upper critical field

The magnetization was measured for the same samples used in the hysteresis measurements. Fields from 500 Oe to 5 Tesla were applied. At each field, the temperature

was varied from 10 K to 300 K, while the magnetization data was measured (Table 3-2).

For reliable measurements in reversible region, a half-minute pause was used to stabilize the set temperature before taking the measurement. Ideally, when the temperature is above T_c, the sample should be in normal state, and the magnetization is very small compared to superconducting state. However, thermal fluctuation and other factors must be accounted for to correct H_{c2} correctly. Therefore, the normal state magnetization of the Eu magnetic momentum must be corrected for in the Hao-Clem Model [28]. Various corrections were tried including Curie-Weiss Law at low field, by Brillouin function or modified Brillouin function over wide field region. Some data needed other mathematics correction. For example, M vs. T raw data curve of $Bi_2Sr_2Ca_2Cu_3O_{10}$ at high temperature can be fitted by means of Curie-Weiss law [36]. M vs. T curve of Y123 stoichiometric sample can be fit with Curie-Weiss type magnetization functions [37]. However for EuLR123, Eu atom has a low excitation energy level, which is very close to the ground state [9]. At high temperature, this second energy level will be partially occupied and the net magnetic moment is not zero. The magnetization data of Eu123 does not have Curie-Weiss behavior.

Table 3-2 The SQUID sequence for magnetization measurements

Temperature range	Step size
10 ~60 K	10K
61~100K	1K
105~140K	5K
150~300K	10K

* Applied field s: 500 Oe, 2000 Oe, 5000 Oe, 1 T, 2 T, 3 T, 4 T, 5 T

Due to the complexity of the background correction, alternative way is to subtract the normal state magnetization data of the deoxygenated sample for each composition. Removal of the oxygen will not decompose the structure, therefore the rare earth magnetic momentum should be identical to the fully oxygenated sample. Since O atom has no magnetic momentum, their removal will not change the background.

This background correction has proved difficult. Six different approaches were tried. The one described in the following worked well.

For the data M vs. H data, there is about 1% deviation in slope between the oxygenated and deoxygenated sample at high fields ($\geq$ 3 Tesla). The difference in slope can be due to systematic measurement error in mass and field. The slopes and intercepts for the high field ($\geq$ 3 Tesla) data at each temperature were determined for the deoxygenated and oxygenated sample. The ratio of these two corresponding slopes above 140 K, where the fluctuation is negligible, was almost constant. The average of the slope ratios above 140K was used as a correction factor. The correction factor was multiplied to the deoxygenated data and then this corrected data is subtracted from the raw oxygenated data. In some samples, small amounts of ferromagnetic contributions were observed, so the intercepts were corrected according to the specific offset for each sample.

CHAPTER 4. RESULTS AND DISCUSSIONS

4.1 Crystal Structure of $Eu(Ba_{1-x}Nd_x)_2Cu_3O_{7+\delta}$

The DTA results of the series of $Eu(Ba_{1-x}Nd_x)_2Cu_3O_{7+\delta}$ shows that these samples are phase pure after repeated high temperature anneals. The temperature of the peritectic decomposition reaction versus the doping level (Figure 4.1) does not have abrupt change. The temperature decreases smoothly with the increase of x, which implies that the samples are continuous solid solution.

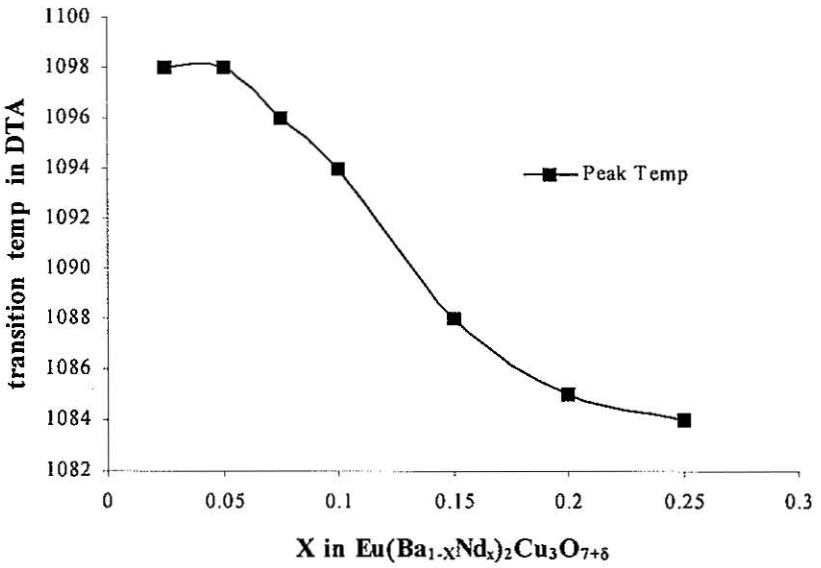

Figure 4.1 The peritectic decomposition temperature versus the doping level

X-ray data show that most of the samples are single phase with all the peaks indexed to the 123 crystal structure. Although a few samples have a very tiny amount of a second phase, it is so little to influence the measurement results.

The lattice parameters of $Eu(Ba_{1-x}Nd_x)_2Cu_3O_{7+\delta}$ for $0 \leq x \leq 0.25$ are shown in Figure 4.2a. The a-axis expands gradually with the increase of doping level while the b-axis shrinks gradually as expected. At x = 0.13, the a-axis and the b-axis converge and the crystal structure changes from orthorhombic to tetragonal. With further increase in x, the a-axis of the tetragonal structure begins to decrease. Figure 4.2b shows that the c-axis decreases with increasing x, since Nd^{3+} is smaller than Ba^{2+}. Likewise, the volume (Figure 4.2c) decreases monotonically with x increasing.

In order to explore the topic more deeply, all the data for EuLR123ss, LR = La, Pr, Nd and Eu were combined together. Figure 4.3a shows the a and b-axes for the four series of samples. Obviously, our data for Nd series is consistent with the other data. The ionic sizes of La^{3+}, Pr^{3+}, Nd^{3+}, Eu^{3+} are 1.061Å, 1.013 Å, 0.995 Å and 0.95 Å, respectively. After substitution, Eu addition depresses the b-axis and enhances the a-axis more quickly than the other three series. The a-axis of the tetragonal structure of $Eu(Ba_{1-x}Eu_x)_2Cu_3O_{7+\delta}$ being the smallest of all rare earth and on the contrary, La^{3+} be having the largest ionic size, its lattice parameters change more slowly with increasing x compared to the other series. The other two series with Pr and Nd substitutions also follow the trend of ionic size and doping level controlling lattice size and the orthorhombic /tetragonal (O/T) transition. Figure 4.3b and Figure 4.3c show the trend of the c-axis and volumes for all the specimens. Orthorhombicity (Figure 4.4), which shows the concentration of O/T transition is determined by

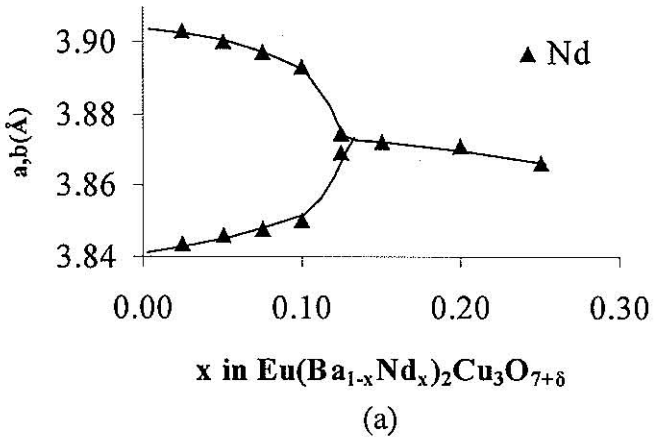

(a)

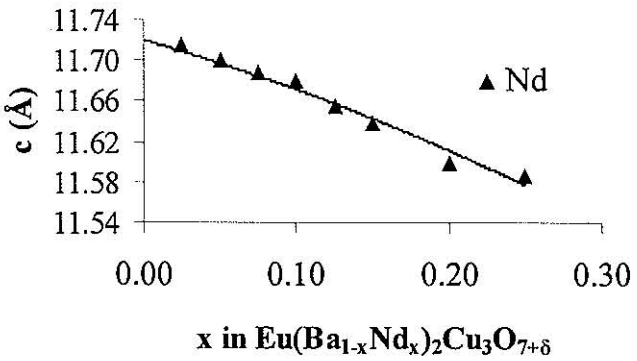

(b)

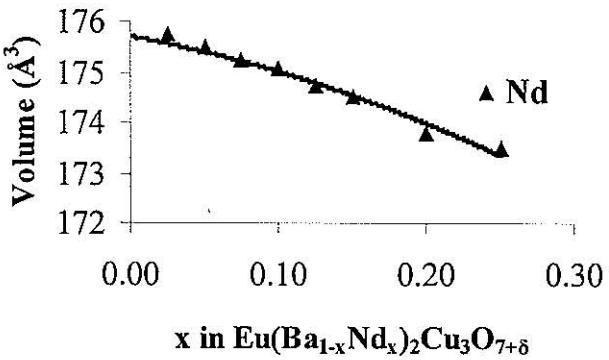

(c)

Figure 4.2 The lattice parameters of $Eu(Ba_{1-x}Nd_x)_2Cu_3O_{7+\delta}$
(a) a, b axis; (b) c axis; (c) volume

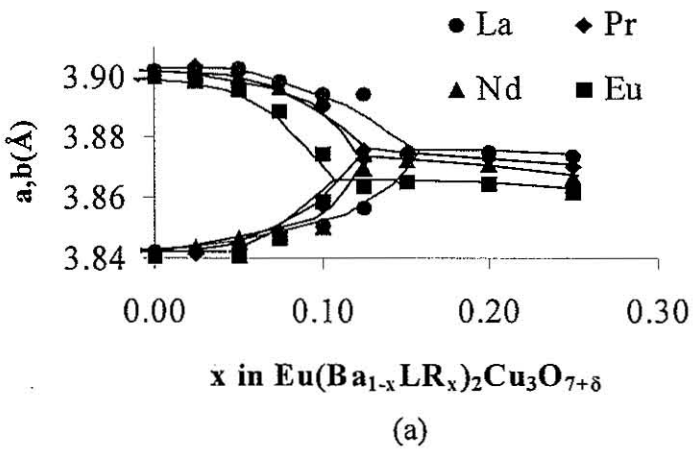

(a)

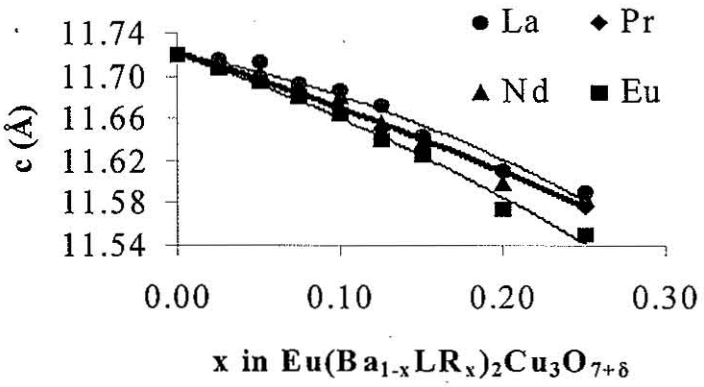

(b)

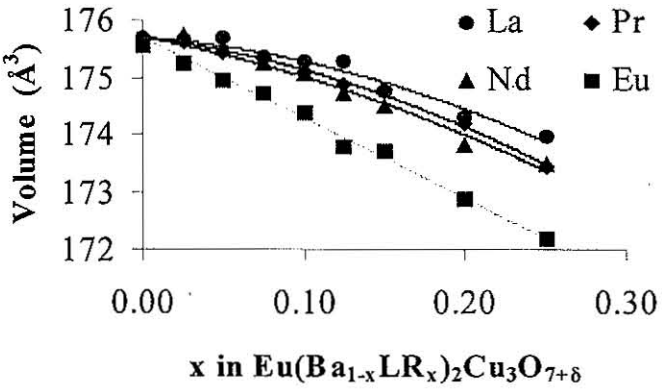

(c)

Figure 4.3 The lattice parameters of Eu $(Ba_{1-x}LR_x)_2Cu_3O_{7+\delta}$
(a) a, b axis ; (b) c axis; (c) volume

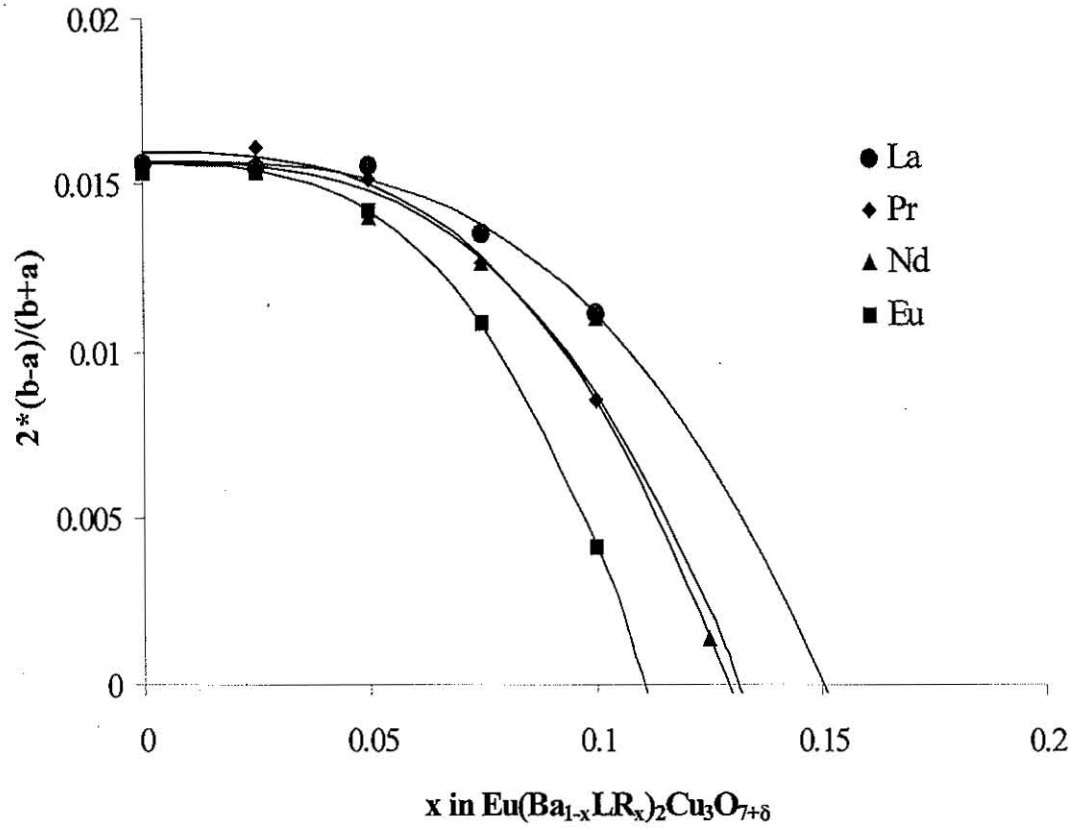

Figure 4.4 The orthorhombic /Tetragonal transition curve of Eu $(Ba_{1-x}LR_x)_2Cu_3O_{7+\delta}$

$$O = \frac{2*(b-a)}{b+a} \qquad \text{equ. (4.1)}$$

The critical concentrations for La, Pr, Nd, La series are x = 0.15, 0.13, 0.13, 0.11, respectively. Because Pr^{3+} and Nd^{3+} has similar ionic radii, their lattice parameters and O/T transition curves almost overlap.

4.2 Critical Transition Temperature of $Eu(Ba_{1-x}Nd_x)_2Cu_3O_{7+\delta}$

The T_cs of all the EuLR123ss samples are shown in Figure 4.5a. The zero-field cooled curves are characterized using the 10%, 50%, 90% points of the full diamagnetic signal curve with an applied field of 10 Oe. In Figure 4.5a only the midpoints (50% points) of all the corresponding curves are plotted. Unlike the lattice parameters, the T_c behavior of EuLR123ss can not be explained only with ionic size effects. For example, Pr^{3+} ion size is between that of Nd^{3+} and La^{3+}, but it depresses T_c much faster than the other three elements. Evidence shows that the suppression of superconductivity is unlikely due to mixed valence of Pr on Ba site [17]. It was also proposed that the faster depression of superconductivity by Pr is caused by a unique change in the electron structure such as the hybridization of Pr 4f-O 2pπ or interaction of the crystal field split energy levels [17]. The transition temperature width of EuNd123ss and EuEu123ss, using the difference between the 10% and 90% transition points of the zero-field cooled curve, is shown in Figure 4.5b. The T_cs of Nd and Eu series are on top of each other. This suggests that the moment of the LR ion does not affect the depression in T_c.

4.3 Critical Current Density of $Eu(Ba_{1-x}LRx)_2Cu_3O_{7+\delta}$

The effect of the dopants and doping level on the flux pinning is investigated next. In the lightly doped region, $x \leq 0.05$, the T_c of EuLR123ss is nearly constant.

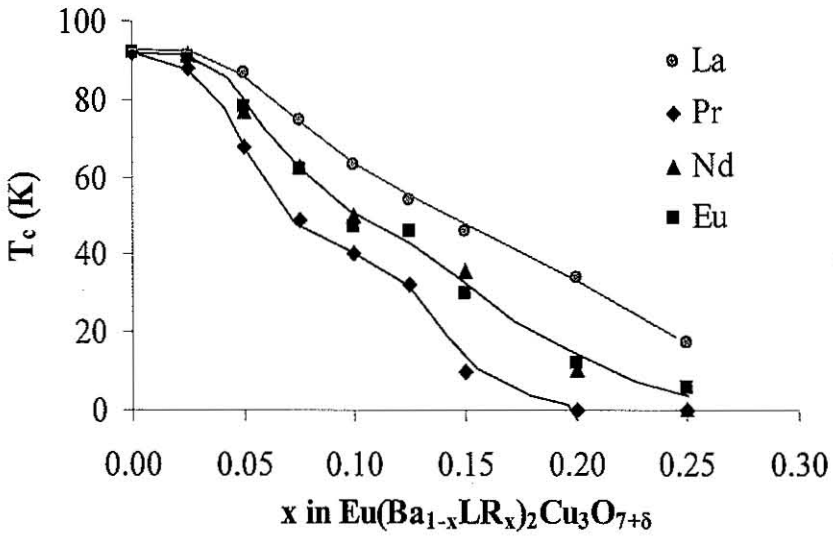

(a)

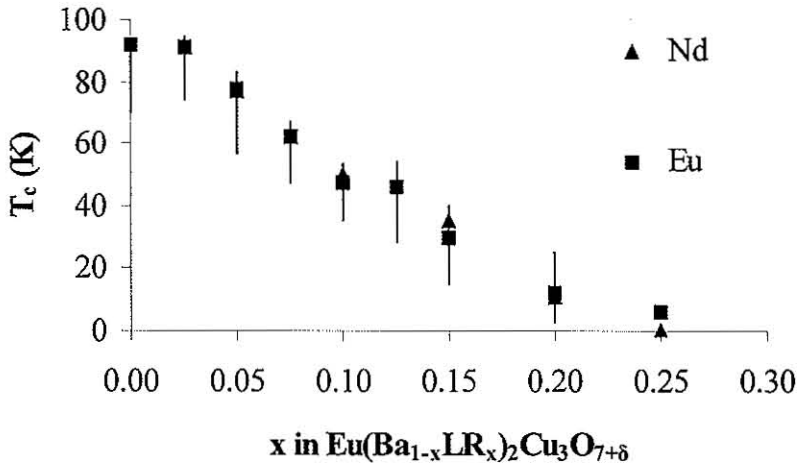

(b)

Figure 4.5 (a) the T_cs of $Eu(Ba_{1-x}LR_x)_2Cu_3O_{7+\delta}$; (b) the transition temperature width of $Eu(Ba_{1-x}LR_x)_2Cu_3O_{7+\delta}$

It is known that small defects whose size is comparable to the coherence length ξ may pin flux more strongly than larger defects. In light of their high T_cs and small defect sizes, lightly doped samples were investigated. As mentioned in equation (2.7), the critical current density is proportional to $\frac{\Delta M}{d}$. In order to amplify the effect caused by the small difference in defects size and density, $\log(\frac{\Delta M}{d})$ was used in the comparisons. At this moment, we are only interested in the relative instead of the absolute values. In addition, J_c is also a function of temperature and field, decreasing with the increase of temperature or applied field. The critical current density of the stoichiometric Eu123, EuLa.025, EuLa.05, EuPr.025, EuPr.05, EuNd.025, EuNd.05, EuEu.025, EuEu.05 are depicted in Figure 4.6 through Figure 4.10.

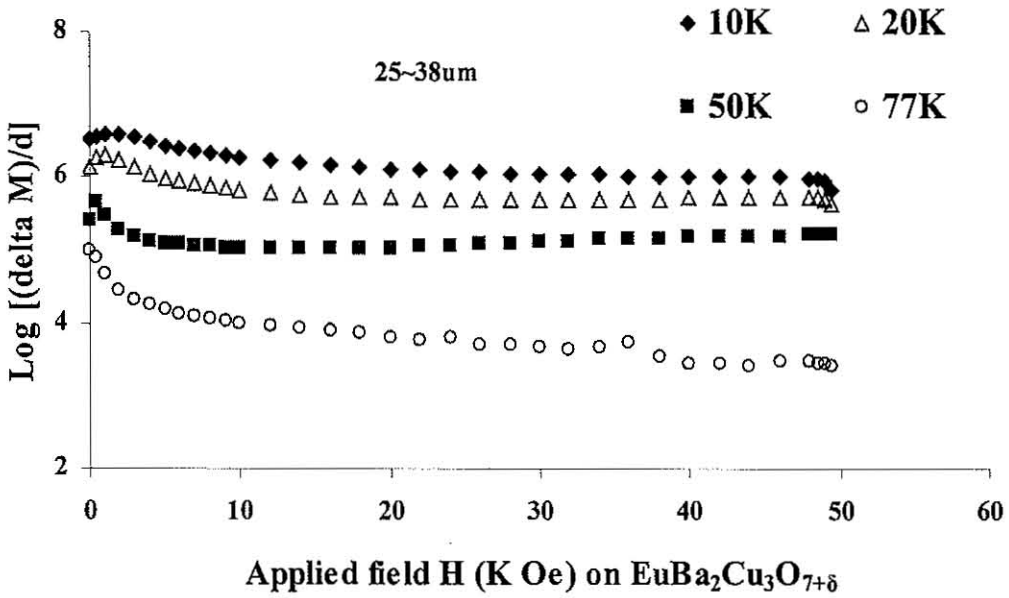

Figure 4.6 The Jc of $EuBa_2Cu_3O_{7-\delta}$ at different temperatures and fields.

Above the applied field, where the samples show a granular behavior ($H \geq 0.5T$), some samples exhibit "fishtail effect" [24,25], where the J_c increase with increasing field. This effect is due to the pinning site spacing, which corresponding with the vortex lattice. The $\log\left(\frac{\Delta M}{d}\right)$ vs. composition at 4T applied field are shown in Figure 4.11. The four different curves are for temperatures of 10K, 20K, 50K and 77K. At 10K and 20K, it was observed that the smaller the substitution atom, the higher the J_c at $x = 0.025$, i.e. Eu123 < EuLa.025 < EuPr.025 < EuNd.025 < EuEu.025. At higher temperature and higher doping level, the ionic size effect of J_c is no longer dominant.

4.4 Irreversibility Line of $Eu(Ba_{1-x}LRx)_2Cu_3O_{7+\delta}$

In order to determine the magnetic properties correctly, we need to isolate the measurement artifacts and correct the background. For example, in the randomly oriented stoichiometric Eu123, the small amount of magnetic moment of the Eu atom contributes to the background. Due to the complexity of all the terms contributing to the background, measurements of background terms are performed then subtracted. For example, deoxygenated Eu123 was measured to determine the normal state paramagnetic moment since O has no magnetic moment and the number of Eu atoms does not change. Although these two samples should have the same background magnetization, because of the measurement errors, we can not subtract them directly. Using the fits to the slope of M vs H, which were described in detail in Chapter 3, the slope and intercept were measured. The slope difference arises from the mass error and the non-zero intercept is from the

ferromagnetic impurities in the deoxygenated sample. After correcting these two factors, subtraction was made. The corrected magnetization of stoichiometric Eu123 is shown in Figure 4.12. It is clear that there are two crossing points, 93.25 K at low fields and 92K at high fields. After correcting the background, it would be possible to determine H_{c2} if the sample were isotropic. Due to the difficulty to correct the background of the aligned sample, it is difficult to determine H_{c2}. However, it is still useful to at least know the field dependence of the irreversible line. Therefore, T_c/T_{co} vs. H curve were studied. However, the field dependence of the irreversible line is strongly dependent on crystallographic orientation. Therefore, the sample powders had to be aligned.

The background of the lightly doped EuLR123ss will not change too much from the stoichiometric Eu123 since the contribution of the extra rear earth is negligible. The samples used are Eu123, EuLa.025, EuLa.05, EuEu.025, and EuEu.05. Using the methods described in Chapter 3, grain alignment was performed for each sample. XRD of the sample shows that all of the samples have good c-axis alignment except EuEu.05 (Figure 4.13), confirming that at room temperature the Eu moment on RE sites has its easy axis in a-b plane. The loss of c-axis alignment for EuEu.05 suggest that the easy axis is along c–axis. These two moments compete with each other. With increasing the Eu content on the Ba site, a threshold value is passed and the anisotropy along c–axis becomes larger than that in a-b plane and c–axis alignment along the applied field becomes more energy favorable. In order to verify this assumption, we applied a field perpendicular to the sample surface without rotation (Figure.4.14). The XRD data shows good c-axis alignment. After achieving good grain alignment, background corrections were attempted.

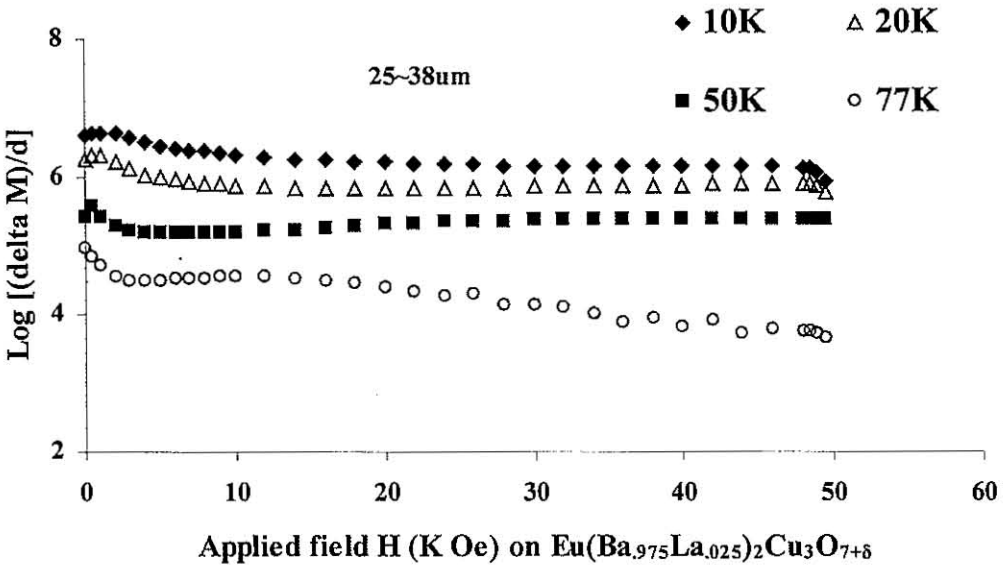

(a)

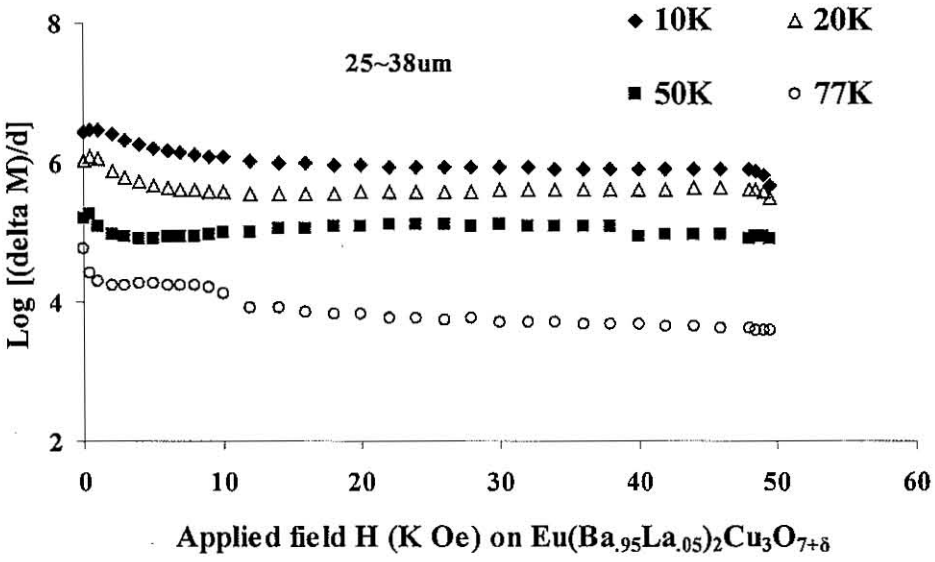

(b)

Figure 4.7 The J_c of (a) $Eu(Ba_{.975}La_{.025})_2Cu_3O_{7+\delta}$; (b) $Eu(Ba_{.95}La_{.05})_2Cu_3O_{7+\delta}$ at different temperatures and fields.

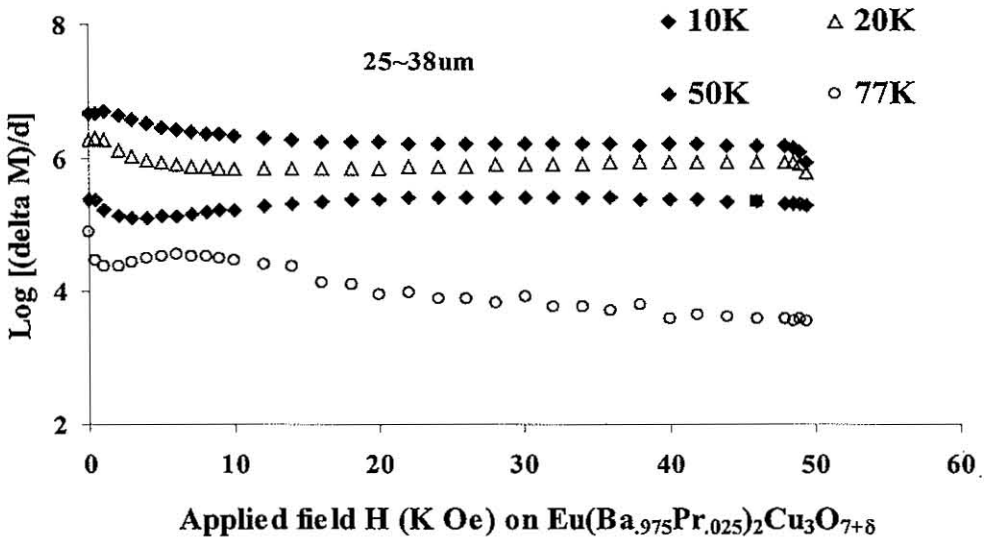

(a)

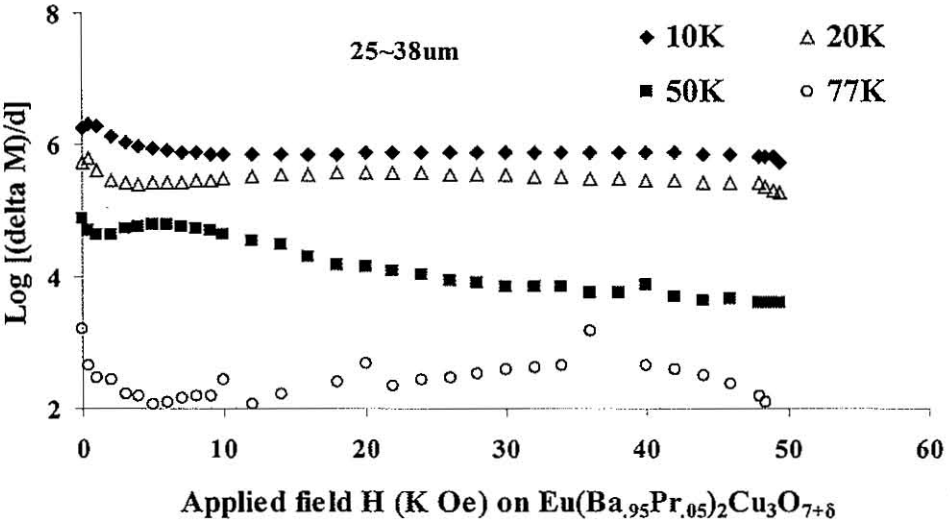

(b)

Figure 4.8 The J_c of (a) $Eu(Ba_{.975}Pr_{.025})_2Cu_3O_{7+\delta}$; (b) $Eu(Ba_{.95}Pr_{.05})_2Cu_3O_{7+\delta}$ at different temperatures and fields.

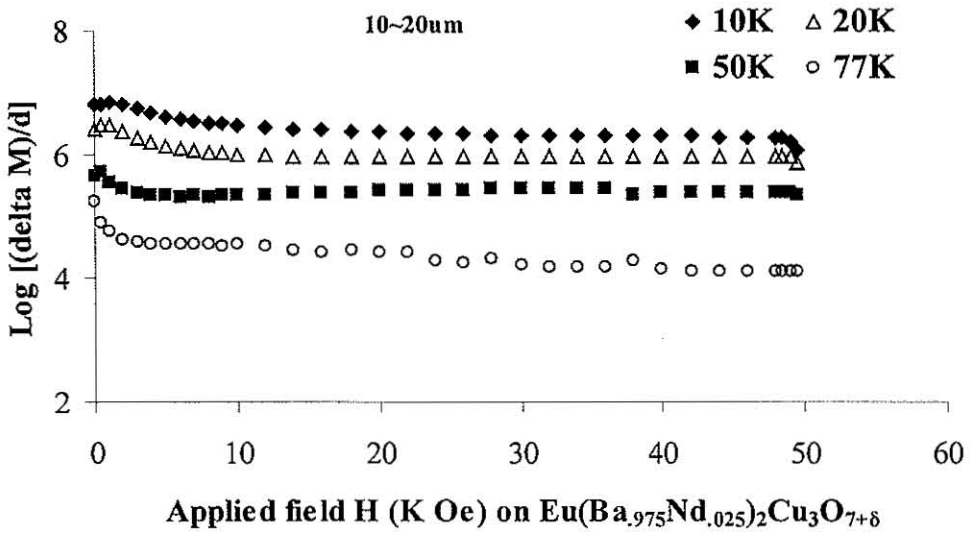

(a)

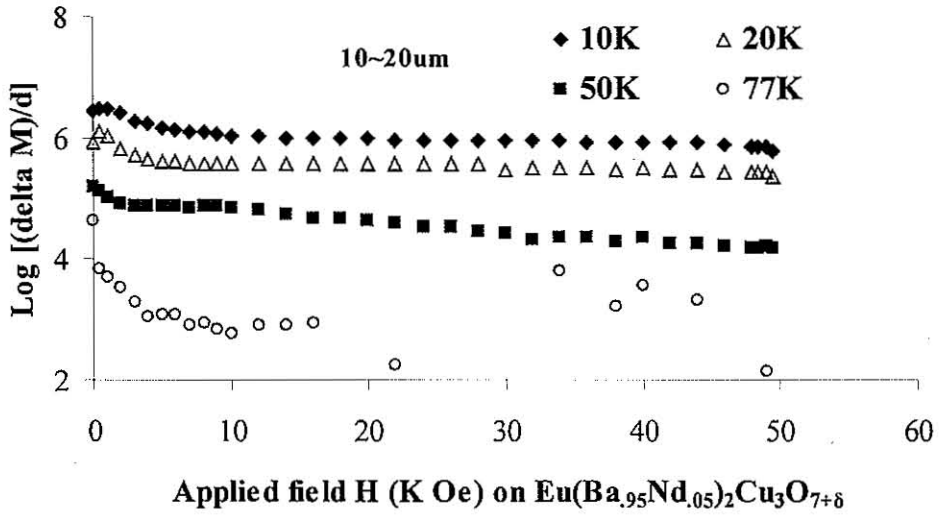

(b)

Figure 4.9 The J_c of (a) $Eu(Ba_{.975}Nd_{.025})_2Cu_3O_{7+\delta}$; (b) $Eu(Ba_{.95}Nd_{.05})_2Cu_3O_{7+\delta}$ at different temperatures and fields.

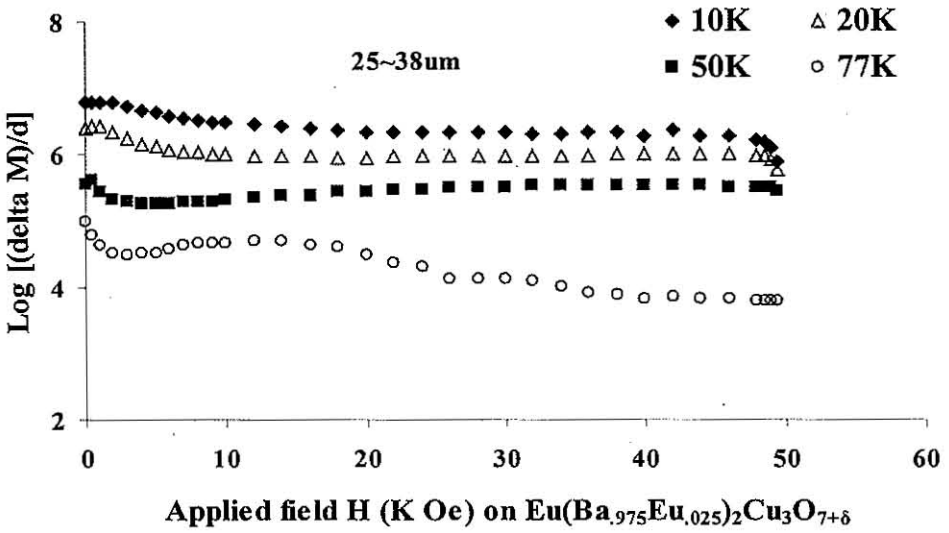

(a)

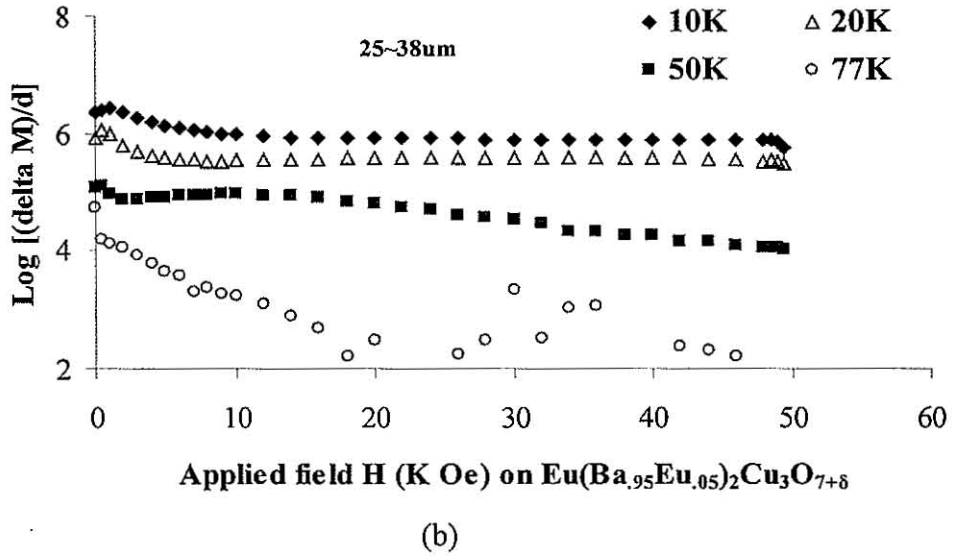

(b)

Figure 4.10 The J_c of (a) $Eu(Ba_{.975}Eu_{.025})_2Cu_3O_{7+\delta}$; (b) $Eu(Ba_{.95}Eu_{.05})_2Cu_3O_{7+\delta}$ at different temperatures and fields.

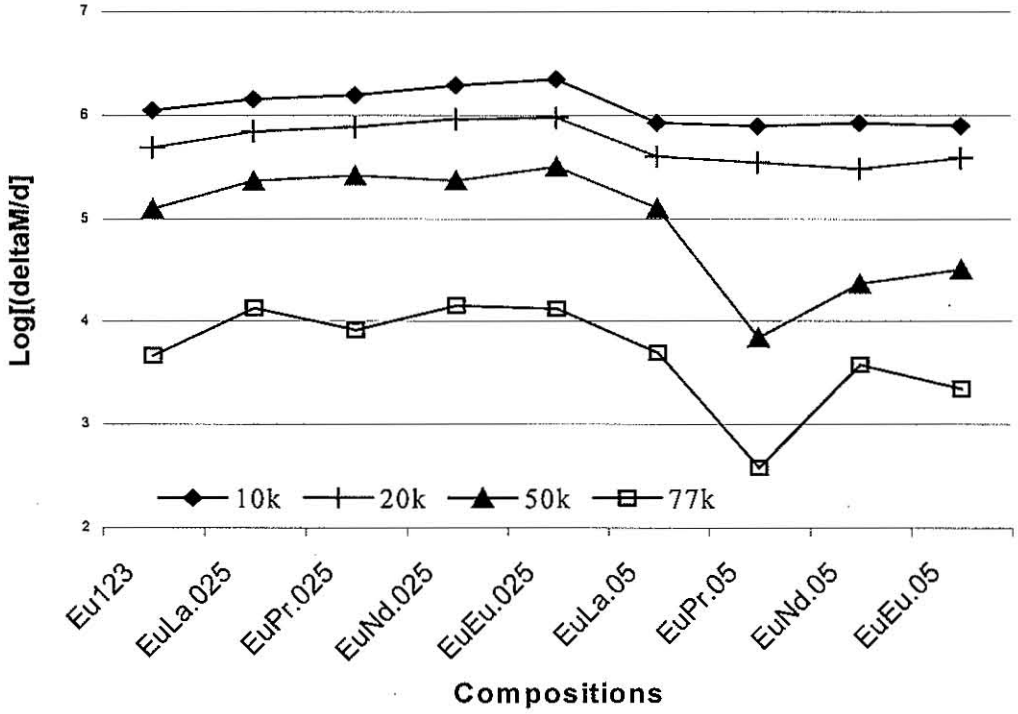

Figure 4.11 The J_cs of different compositions at 4T applied field and different temperatures.

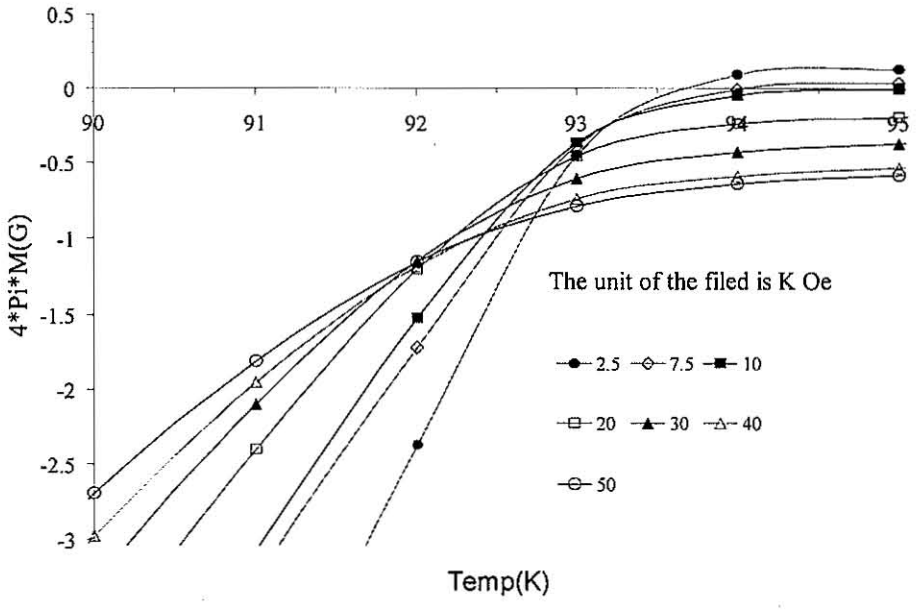

Figure 4.12 The magnetization of $EuBa_2Cu_3O_7$

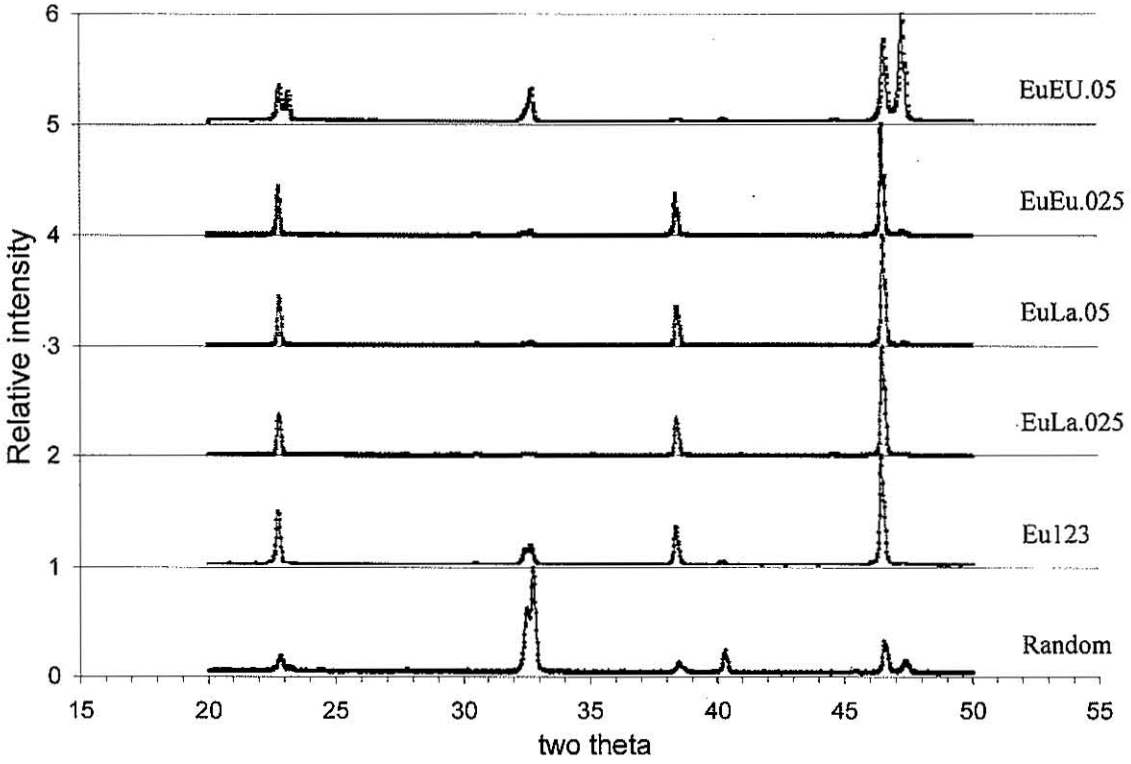

Figure 4.13 The x-ray patterns for EuLR123

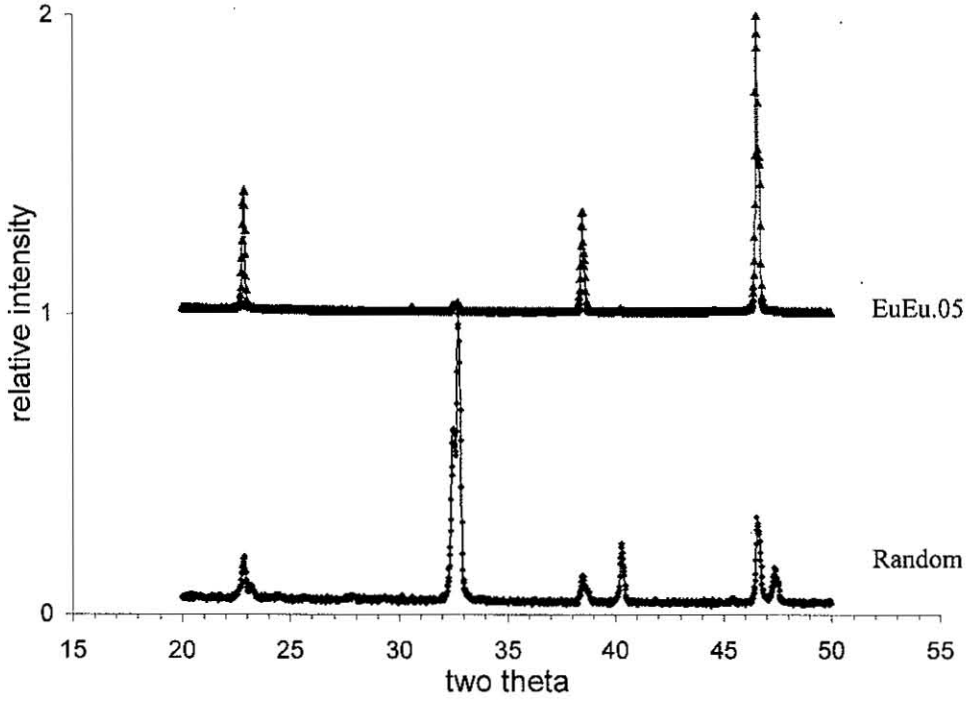

Figure 4.14 The x-ray pattern of Eu Eu.05 and random oriented Eu123

Unfortunately, in addition to the Eu moment, we have other background contributions, like the diamagnetic cubic Cu holder. When the powder and epoxy were mixed outside of the Cu cube, there are mass errors due to variability in mixing density and homogeneity of the powder-epoxy mix. All of these factors make the corrections hard. The magnitude of the magnetization in the region of interest is comparable to the errors introduced by the background subtraction. The magnetization of a sample with H||C has three terms. First is the magnetization of the sample itself (M_s) and the other are those from Cu (M_{cu}) and epoxy (M_{epx})

$$M_{H\|c}=M_{sH\|c}+M_{cu}+M_{epx} \qquad \text{equ. (4.1)}$$

For the same sample, the magnetization of H⊥C can be expressed as

$$M_{H\perp c}=M_{sH\perp c}+M_{cu}+M_{epx} \qquad \text{equ. (4.2)}$$

The difference between these two directions should remove the artifacts from the Cu and epoxy

$$M_{H\|c} - M_{H\perp c} = M_{sH\|c} - M_{sH\perp c} \qquad \text{equ. (4.3)}$$

These results show the irreversible to reversible (irr /re) transition more clearly than the raw data of each orientation. Therefore, the exact T_{irr} temperature can be easily determined. The difference of the magnetization for the two directions enhances the kink in the magnetization at the transition, as was shown in the slope of the magnetization vs. temperature plot near T_c (Figure 4.12). By fitting the slopes at a temperature far below and far above T_c, the crossing of two slopes near T_c were observed. The magnetization vs. temperature at 1T applied field for four different compositions is shown in Figure 4.15 and T_{irr} given in Table5-1. In terms of reduced temperature, T_{irr}/T_c, which is the ratio of T_{irr} and

T_c, the corresponding values for Eu123, EuEu.025, EuLa.025 and EuEu.05 are 0.98, 0.96, 0.93 and 0.885 respectively.

Here, T_c was determined from M (T) measurements at each field. T_{co} is the T_c at 500 Oe. Around T_c, the sample is in fluctuation region and the slope changes gradually. When the magnetization changes sign, the S/N ratio is very small and the magnetization measurements are ill defined around this region. Because of the measurement noise, the slopes of every three points were taken to smooth the curve. Around T_c, the curve is quite linear and when the temperature approaches T_c, the slope approaches zero. The width of the transition is determined by the two crossing points of the 3 linear segments of the slope vs. Temperature curve and the mid-point of these two points is taken as T_c for this experiment. Figure 4.16(a) shows the T_c/T_{co} vs. H curve of these samples. For every applied field above zero, T_c for H⊥C is larger than H||C. This is expected because the currents flow more readily in the Cu-O plane. However, for H⊥C, part of the current path has to go from one layer to another layer, which it is more difficult than within the layer, resulting in intrinsic pinning. For this reason, the T_c depression of H||C is larger than that with H||C at the same applied field. The T_c/T_{co} vs. H curve of EuEu.025, EuLa.025, EuLa.05 are illustrated in Figure 4.16.

It is also observed that Eu123 has the smallest T_c depression at the same applied field than the other compositions. EuLa.05 has higher T_c depression than EuLa.025 no matter the applied field is parallel or perpendicular to the c-axis [Figure 4.17].

These results indicate that the point–like-defects caused by rare earth ions on the Ba site are not effective at pinning the flux lattice near the irreversibility line. Although the critical current is enhanced far away from this region of flux melting, the thermal motion of the flux lattice near T_c is too large to be pinned by these types of defects.

Table 5-1 The data of the T_{irr} and T_c at 1T applied field

	T_{irr} (K)	T_c(K)	T_{irr}/T_c
Eu123	90	92	0.98
EuEu.025	87	91	0.96
EuLa.025	84	90	0.93
EuEu.05	77	87	0.885

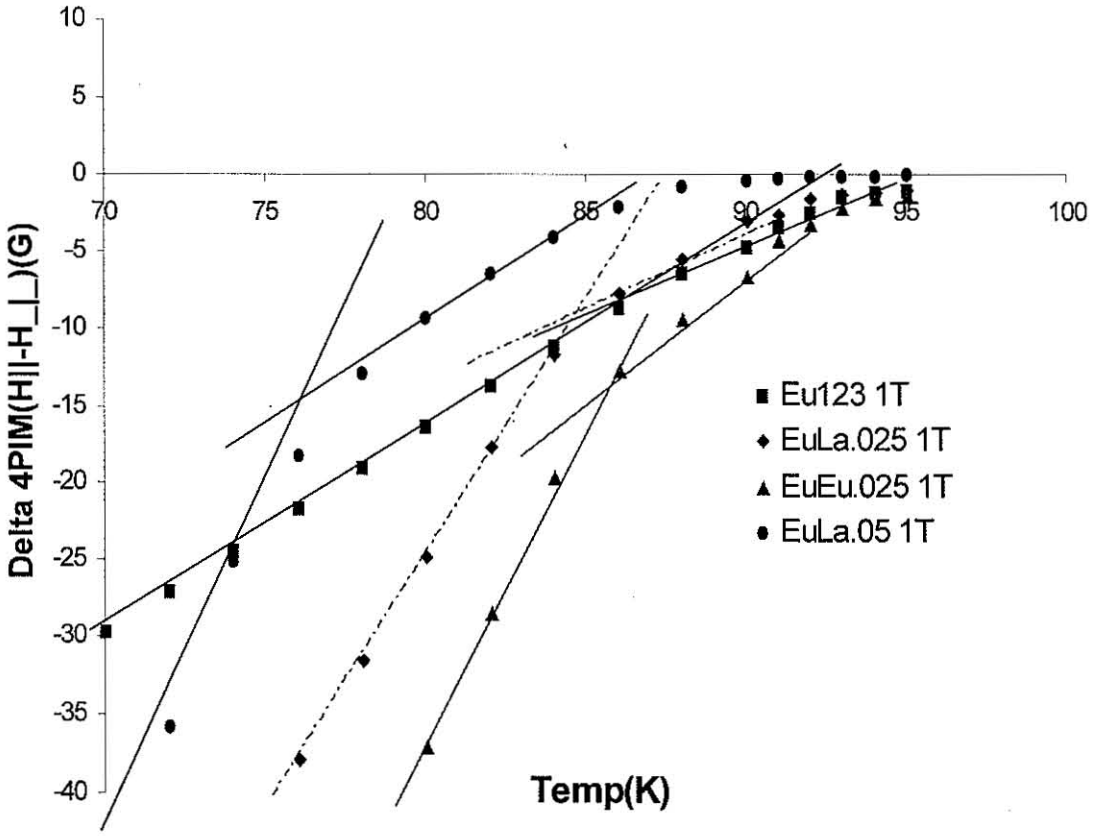

Figure 4.15 The magnetization of EuLR123

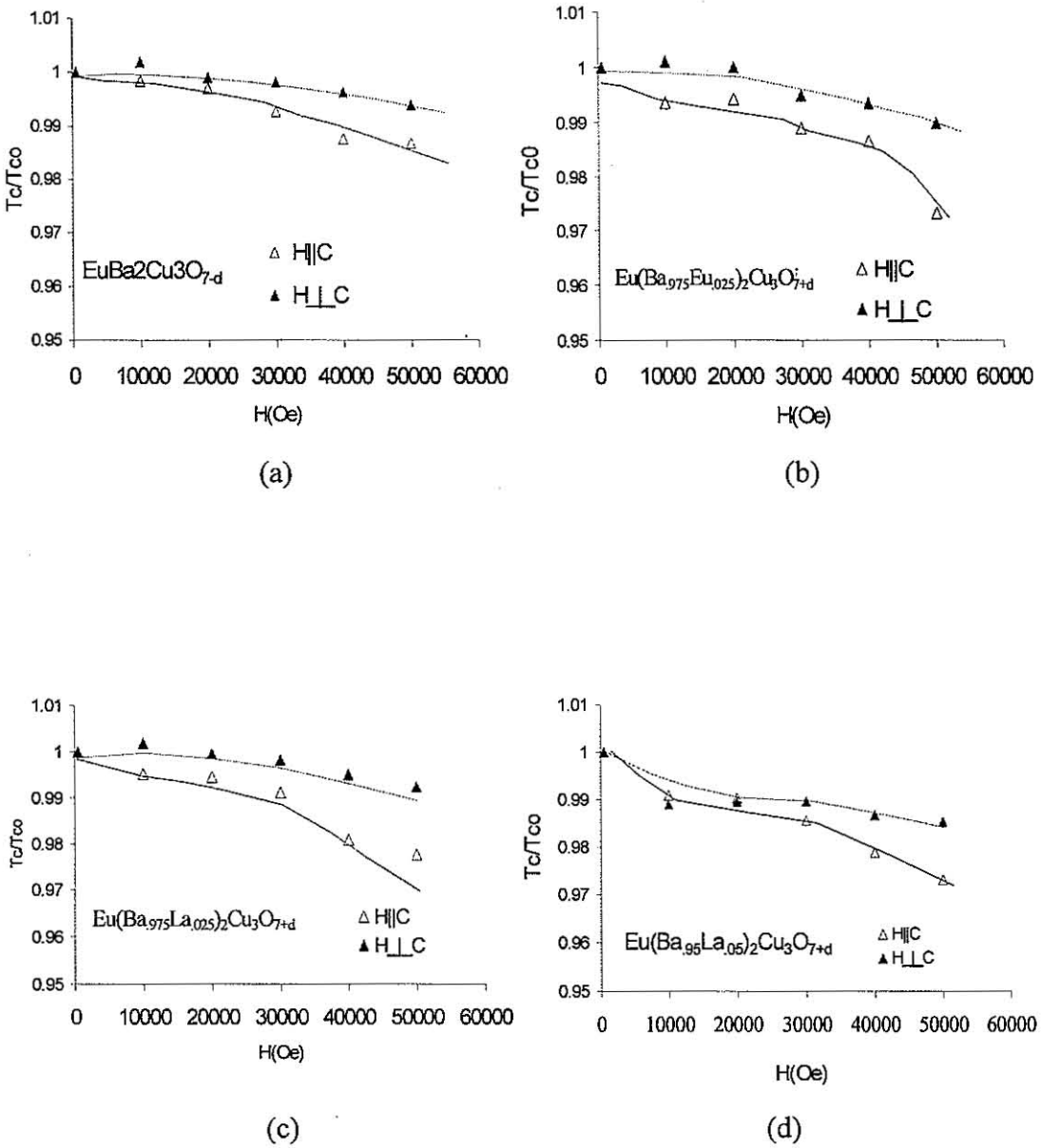

Figure 4.16 The T_{co} depression of (a) Eu123; (b) EuEu.025; (c) EuLa.025; (d) EuLa.05

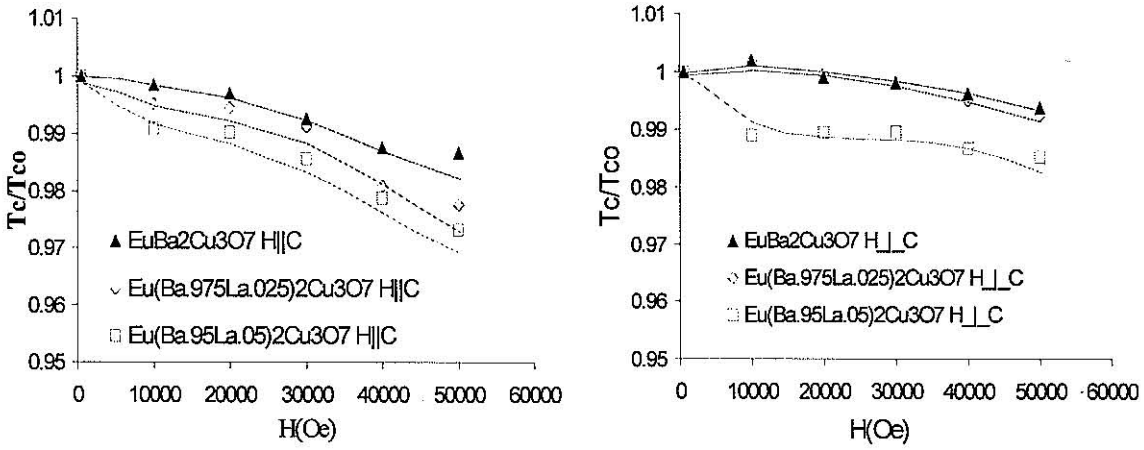

Figure 4.17 The Tc depression of EuLR123 (a) H||C; (b) H⊥C

CHAPTER 5. CONCLUSIONS

An investigation of the role of LR^{3+} substitution on Ba^{2+} lattice sites in the 90 K superconductor $EuBa_2Cu_3O_{7-\delta}$ was carried out in order to quantitatively determine the thermodynamic parameters associated with the depression of T_c with increasing x in $Eu(Ba_{1-x}LR_x)_2Cu_3O_{7+\delta}$. In order to achieve this goal, it is necessary to prepare extremely high quality samples, and determine the difference in magnetization between the superconducting and normal state. In addition, the role of the LR^{3+} magnetic moment should be separated from ionic size effects.

This thesis is comprised of two parts, the synthesis and characterization of Nd and La doped $Eu(Ba_{1-x}LR_x)_2Cu_3O_{7+\delta}$ and the understanding of the superconducting properties of these systems. In order to separate role of ionic size, charge and magnetic moment of the substituting trivalent rare earth ions in place of divalent Ba in light rare earth 123 compounds, a systematic substitution of La, Pr, Nd and Eu onto the Ba site in Eu123 was performed. The work was, in part, a continuation of previous research [17].

The materials synthesis work involved using carefully controlled ceramic processing to produce high quality samples of $Eu(Ba_{1-x}Nd_x)_2Cu_3O_{7+\delta}$ with $0.025 \leq x \leq 0.25$. These samples compliment other samples with other light rare earth substitutions of the Ba^{2+} which had previously been prepared. The samples were characterized using Differential Thermal Analysis (DTA) and powder X-ray diffraction. The DTA results show a single endothermic event at the peritectic decomposition temperature indicating that the samples are free of CuO_2 and $BaCu_2O_3$. The peritectic decomposition temperature is a monotonic function of

the doping level consistent with the behavior of a single phased solid solution. Rietveld refinement of the XRD data shows that Nd substitutes only for the Ba. It is clear that the a-axis expands and b-axis shrinks gradually when x is increasing. At x = 0.13, the a-axis and b-axis converge and the crystal structure changes from orthorhombic to tetragonal. With further increase in x, the a-axis of the tetragonal lattice decreases. In both orthorhombic and tetragonal cells, the c-axis and volume also shrink monotonically with x increasing.

The trends of the lattice parameters of $Eu(Ba_{1-x}Nd_x)_2Cu_3O_{7+\delta}$ are consistent with the other EuLR123ss series, LR = La, Pr, Eu and they can be easily explained with ionic size effects. The ionic size of Ba^{2+} is 1.34 Å while that of the LR^{3+} ion decreases monotonically with increasing atomic number with La^{3+}, Pr^{3+}, Nd^{3+} and Eu^{3+} having radii of 1.061, 1.013, 0.995 and 0.95 Å, respectively. In the orthorhombic structure, the difference in a and b lattice parameters decreases with increasing x in all cases. The rate of the decrease increases with decreasing size of the LR^{3+} ion so that the critical concentration for the orthorhombic to tetragonal transition decreases from La to Eu, (La, x = 0.15) > (Pr $\approx$ Nd, x = 0.13) > (Eu, x = 0.11). The c-axis and unit cell volume decrease monotonically from La to Eu.

The superconducting properties were characterized using DC SQUID magnetometry. Unlike the uniform change in lattice parameter, the superconducting transition did not vary systematically with the ionic size of the dopants. Although the general trend was for the depression of T_c to increase with decreasing ionic size of the dopant for the same doping level, Pr was anomalous, depressing T_c faster. Although the exact mechanism is not clear, this result is consistent with the depression of T_c for Pr substitution for the rare earth in R123.

The critical current J_c was determined using the Bean model from magnetization versus field measurements as a function of temperature and field and the effect of the dopants

on the decrease of J_c with the increasing of temperature or applied field was determined. For $T < 77$ K and small values of x, the value of J_c increased over that of the $x = 0$ sample. In addition, the smaller the substituting atom, the higher the J_c becomes. For instance, at $x = 0.025$, Eu123 < EuLa.025 < EuPr.025 < EuNd.025 < EuEu.025. The enhancement of J_c disappears for $x > 0.05$ and $T > 0.5T_c$.

In order to determine the value of the upper critical field, H_{c2}, or calculate the value of the thermodynamic critical field, H_c, from magnetization data, the difference in magnetization between the normal and superconducting states must be accurately known. Thus the determination of the normal state magnetization below T_c is critical. Due to the Eu moment, which arises from the fact that its ground state is not purely a Hund's rule ground state, the normal state magnetization versus temperature is not easily modeled. It was found that for randomly oriented powders, the normal sate magnetization could be determined from the deoxygenated sample if suitable corrections were made. This allowed the determination of the upper critical field near the superconducting transition temperature.

The thermodynamic critical field, H_c, for a type II superconductor can be determined using the Hao-Clem model. Unfortunately for anisotropic materials, the model may only be applied to single crystal or grain oriented polycrystalline materials. The preparation of uniformly doped single crystals is exceptionally difficult and beyond the scope of this work. Therefore collections of single grain particles were oriented in a magnetic field at room temperature. For Eu123, the anisotropy in the room temperature magnetization is such that the c-axis aligns perpendicular to an applied field. Thus, in order to obtain a c-axis aligned sample it was necessary to rotate the sample about an axis perpendicular to the applied field during alignment. Although very highly aligned samples were obtained, the alignment

process introduced added contributions to the magnetization due to the epoxy and Cu cube which were used. These contributions introduce an uncertainty in the background correction on the order of 0.1% of the change in magnetization associated with the superconducting transition. Unfortunately near T_c this uncertainty is too large for the successful application of the Hao-Clem model.

The aligned samples did allow for the determination of the anisotropy in T_c and the temperature dependence of the irreversibility line near T_c. For a field of 1 T, the temperature below which the magnetization was irreversible, T_{irr}, was 0.98 T_c for undoped Eu123. The T_{irr} is 90K, 87K, 84K and 77K, for Eu123, EuEu.025, EuLa.025 and EuEu.05 samples respectively. In terms of reduced temperature T_{irr}/T_c, which is the ratio of T_{irr} and T_c, the corresponding values for Eu123, EuEu.025, EuLa.025 and EuEu.05 are 0.98, 0.96, 0.93 and 0.885 respectively.

In order to compare the anisotropic depression of T_c with magnetic field, $T_c(H)$, T_c/T_{co} was plotted vs. field. The resulting phase diagram shows how the critical transition temperature depends on the applied field. The T_c for H⊥C is always larger than for H||C for all samples. This is because the currents flow primarily along the Cu-O layers. The energy barrier for current to flow between layers results in intrinsic pinning. For this reason, the T_c depression of H||C is larger than that with H⊥C at the same applied field. Stoichiometric 123 has the smallest T_c depression as a function of applied field with the field dependency increasing with increasing dopant levels. These results indicate that the point-like-defects caused by rare earth ions on the Ba site are not effective at pinning the flux lattice near the irreversibility line. Although the critical current is enhanced far away from this region of

flux melting, the thermal motion of the flux lattice near T_c is too large to be pinned by these types of defects.

REFERENCES

1. H. K. Onnes, Leiden Comm, **120b** (1911)

2. J. Schmalian, *Tutorial for 512 Solid State Physics,* Iowa State University, Fall 2000

3. W. Meissner and R. Ochsenfeld, Naturwiss. **21**, 787(1933)

4. J. G. Daunt and K. Mendelssohn, Proc. Roy. Sco (London), **A185**, 225(1946)

5. W. S. Corak, B. B. Goodman, C. B. Satterthwaite, and A. Wexler, Phys. Rev. **96**, 1442(1954); **102**, 656(1956)

6. J. Bardeen, L. N. Cooper and J. R. Schrieffer, Phy. Rev. **108**, 1175(1957)

7. V. L. Ginzburg and L. D. Landau, Zh. Eksp. Teor. Fiz. **20**,1064(1950)

8. C. Kittel, *Introduction to solid state physics*, sixth edition, (New York: Wiley, 1986)

9. M. Tinkham, *Introduction to superconductivity*, (New York : McGraw-Hill, 1975)

10. N. W. Ashcroft and N. D. Mermin, *Solid State Physics*, (New York, Holt, Rinehart and Winston, 1976)

11. T. Sheahen, *Introduction to High-Temperature Superconductivity*, (Plenum Press, New York and London, 1994)

12. D. K. Finnemore, tutorial on *Type1 and type II Superconductors*, Dept. of Physics and Astronomy, Iowa State University

13. A. A. Abrikosov, Zh, Eksp. Teor. Fiz. **32**,1442(1957)

14. R. B. Goldfarb, Demagnetizing factors, In J.evetts(ed.) Concise Encyclopedia of Magnetic and superconducting Materials Pergaamon, Oxford,U.K.,1992

15. Q. Qian, Ph. D dissertation, Iowa State University, 1992

16. M. J. Kramer, S. I. Yoo and R. W. McCallum *et al.*, Phy. C. **219**, 145-155(1994)

17. Y. Xu, M. J. Kramer, K. W. Dennis, H. Wu, A. O'Connor, R. W. McCallum and S. K. Malik, W. B. Yelon , Phy. C. (Amesterdam) **341-348,** 613(2000)

18. R. W. McCallum, H. Wu, K. W. Dennis and M. J. Kramer, High-Temperature and Novel Inorganic Materials, 199(1999)

19. A. A. Abrikosov *et al.*, *Methods of Quantum Field Theory in statistical mechanics* (Prentice-Hall, Englewood, cliffs, NJ:1963)

20. A. I. Liechtenstein and I. I. Mazin, Phys. Rev. Lett. **74**, 1000(1993)

21. M. B. Maple, Appl. Phys. **9**,179(1976)

22. R. Fehrenbacher and T. M. Rice, Phy. Rev. Lett. **70**, 3471(1993)

23. I. I. Mazin and A. I. Liechtenstein, Phys. Rev. B **57**, 150(1998)

24. M. Daeumling, J. M.Seutjens, and D.C. Larbalestier, Nature **346**,332(1990)

25. J. G. Ossandon, J. R. Thompson, D. K. Christen, B. C. Sales et al., Phys. Rev. B **45** 12 534(1992)

26. P. D. Panetta, J. E. Ostenson, and D. K. Finnemore, Phy. Rev. B. **52**,15 570(1995)

27. K. A. Ziqo *et al.*, Phy. Rev. B **60**, 3603(1999)

28. Z. Hao and John R. Clem, Phy. Rev. B **43**, 2844(1991)

29. M. Xu *et al.*, Phy. Rev. B **53,** 15 313(1996)

30. G. J. Dolan *et al.*, Phy. Rev. Lett. **62**, 2184(1989)

31. D. Nelson and S. Seung, Phy. Rev. B **39**,9153(1989)

32. D. S. Fisher *et al.*, Phy. Rev. B **43**,130(1991)

33. T. M. Palstra *et al.*, Phy. Rev. Lett. **61**, 1662(1988)

34. M. McElfresh, *Fundamental of Magnetism and Magnetic Measurements Featuring Quantum Design's Magnetic Property Measurement System*, (Quantum Design,1994)

35. O. Chmaissem, J. D. Jorgensen *et al.*, Nature **397**, 45(1999)

36. Q. Li, M. Suenaga and J.gohng and D.K. Finnemore *et al.*, Phy. Rev. B. **46** 3195(1992)

37. J. Gohng and D. K. Finnemore, Phy. Rev. B **46**, 398(1992)

ACKNOWLEDGEMENTS

I would like to thank my major professors, Dr. R. W. McCallum and Dr. M. J. Kramer, for their patience, kindness and encouragement in leading me into the realm of superconductors. Their positive attitudes toward researches, creative and active thoughts and industrious spirits always impress me, which is my spiritual treasure in my life. Working and studying under their supervision is enjoyable throughout my graduate school years here.

I also thank Dr. Douglas K. Finnemore for the valuable conversations; the time and efforts put on my research. I thank Mr. K .W. Dennis for his great help in my daily experiment, and designing and building the equipment for this research. He also helped train me to use all kinds of equipment. I like to extend my thanks to Mrs. Angela O'Connor for her friendship and assistance in my experiments and daily life here. Special thanks to Dr. Youwen Xu for her great help and advise during my thesis writing and her friendship. I would like also thank Mr. Fran Labbs, Mr. Ning Yang, Mr. Ben Zimmerman, Mr. Michael Foubert and all the people who gave helps for their aids in various occasions.

Finally, I thank my parents and my brother at home for their support. I am also very grateful to my husband, Jinran Chen, for his great love and encouragement so that I could finish this work.

The work at Ames Laboratory was supported by the United States Department of Energy (USDOE), Office of Science (OS), Office of Basic Energy Sciences (BES), through Iowa State University under Contract W-7405-ENG-82.